FISEVIER

Contents lists available at ScienceDirect

# Lithos

journal homepage: www.elsevier.com/locate/lithos



# Mantle melting variation and refertilization beneath the Dragon Bone amagmatic segment (53°E SWIR): Major and trace element compositions of peridotites at ridge flanks



Jixin Wang a, Huaiyang Zhou a,\*, Vincent Salters b, Yang Liu a, Afi Sachi-Kocher b, Henry Dick c

- <sup>a</sup> State Key Laboratory of Marine Geology, Tongji University, Shanghai 200092, China
- b National High Magnetic Field Laboratory, Department of Earth, Ocean and Atmospheric Science, Florida State University, Tallahassee, FL 32306, USA.
- <sup>c</sup> Department of Marine Geology and Geophysics, Woods Hole Oceanographic Institution, Woods Hole, MA 02543, USA.

#### ARTICLE INFO

Article history: Received 22 May 2018 Accepted 16 November 2018 Available online 19 November 2018

Keywords: Southwest Indian Ridge Abyssal peridotites Partial melting Clinopyroxene Refertilization

#### ABSTRACT

The evolution of the mantle melting regime and the process of refertilization beneath cold lithosphere remain ambiguous at ultraslow spreading ridges. Few previous studies were concerned with the temporal variations of mantle melting indicated by peridotites on the flank of a single ridge segment. Here, we present in-situ major and trace element analyses of harzburgites from the Dragon Bone ridge segment both from near the spreading axis and from rift mountains up to tens of kilometers from the ridge axis. We propose that the Dragon Bone mantle had been depleted anciently at higher pressures, prior to the recent ascent under the ridge at lower pressures, and only a limited volume of melt was generated during recent melting beneath the ridge. This interpretation is consistent with the high degree of depletion of the Dragon Bone harzburgites with little trapped melt, and thin discontinuous igneous crust on the seafloor. Comparison of peridotites from near-ridge locations with those further out on the flanks indicates that the melting regime has progressively shrunk over time creating at present a nearly amagmatic segment. Peridotites from segment ends are seldom affected by late-stage refertilization, while those from the segment center are highly depleted mantle residues (resembling those from fast spreading ridges) that sustained *syn*-melting metasomatism.

© 2018 Elsevier B.V. All rights reserved.

#### 1. Introduction

The Southwest Indian Ridge is an ultraslow spreading mid-ocean ridge (Dick et al., 2003), with alternating magmatic and amagmatic spreading modes (Cannat et al., 1999; Dick et al., 2003; Mendel et al., 1997; Standish et al., 2008). In 2010, Chinese RV Dayang Yihao cruise Leg DY115–21 discovered a large area of exposed peridotite with scattered basalts at the Dragon Bone ridge segment at 53°E. This segment was progressively dominated by tectonic extension beginning at 6 Ma, with amagmatic spreading gradually extending from the west to the east (Cheng et al., 2016; Zhou and Dick, 2013). These peridotites can provide direct information about upper mantle. (e.g.: Dick, 1989; Dick et al., 1984; Niu, 2004; Salters and Dick, 2002; Stracke et al., 2011; Warren, 2016), and provide an opportunity to examine its evolution in both time and space.

Several geochemical studies include the Dragon Bone peridotites. Seyler et al. (2003, 2011) analyzed peridotite major and trace elements from 12 dredges from the SWIR between 52°E and 68°E (including one from the Dragon Bone ridge axis) and found mantle heterogeneities on

\* Corresponding author.

E-mail address: zhouhy@tongji.edu.cn (H. Zhou).

multiple levels ranging from the regional- along-axis scale to within individual samples (Seyler et al., 2003). Zhou and Dick (2013) analyzed spinel (Spl) from Dragon Bone DY115-21 peridotites and found their composition significantly depleted, which was unexpected given the scarcity of basaltic crust. Chen et al. (2015) studied the bulk rock major and trace elements of Dragon Bone peridotites, and proposed that the Dragon Bone peridotites had been extensively refertilized and suggested that melt trapped in the mantle may explain the Dragon Bone thin crust. On a more regional scale, Seyler et al. (2003) also found evidence for a modified mantle in the high Na<sub>2</sub>O content of the clinopyroxenes (Cpx). Gao et al. (2016) interpreted the major and trace element variations of Dragon Bone peridotites and basalts as compatible with an ancient melting event of a hydrated mantle wedge above a subducting slab. They recognized two groups of peridotites. One group can be modeled by ~7% fractional melting in the garnet field, followed by ~12-14% melting in the spinel field from either a depleted or a primitive upper mantle. The other group can be modeled by ~15–20% fractional melting in the spinel field from a depleted mantle source.

Neither Chen et al. (2015) nor Gao et al. (2016) considered the spatial-temporal evolution reflected by exhumed peridotites from far to near the axis. Both studies were based on whole rock major and

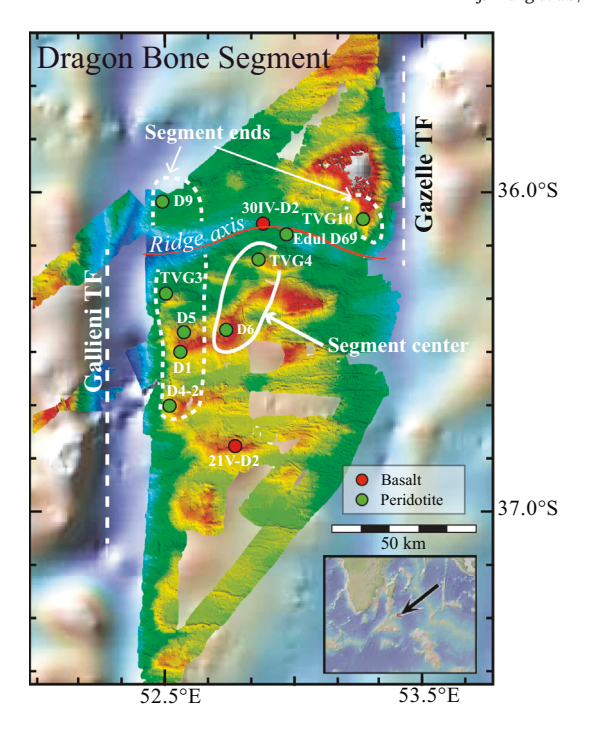


**Fig. 1.** Bathymetric map of the Dragon Bone segment with insert indicating its global location. The green solid circles are peridotites from segment ends and segment center as outlined by dashed lines, and red solid circles represent basalt glasses recovered from this segment. The bathymetric map is revised after Zhou and Dick (2013).

trace element analyses. Interpretation of these results can be difficult due to the large mass fluxes that occur during alteration and weathering in peridotites (e.g., Snow and Dick, 1995). In this paper we use in-situ analyses of trace elements in clinopyroxene, as Cpx are little affected by these processes, to establish the spatial-temporal evolution of partial melting of the Dragon Bone mantle and re-examine evidence for refertilization of the shallow mantle at the end of mantle melting.

# 2. Geological setting and samples

The Dragon Bone segment from 52°20′E to 53°20′E is located on the Southwest Indian Ridge between the 110-km offset Gallieni and 76-km offset Gazelle fracture zones on the west and east, respectively (Fig. 1). This ridge segment is also called the 53°E Amagmatic Segment (Gao et al., 2016; Zhou and Dick, 2013). Sauter et al. (2001) argued that the Gallieni Transform system is a major geochemical and tectonic boundary on the SWIR. To the west of the Gallieni fracture zone lies the

"Dragon Flag" segment, with thicker oceanic crust, which shows extensive hydrothermal activity (Li et al., 2015; Niu et al., 2015; Sauter et al., 2001; Tao et al., 2012; Zhao et al., 2013). In the contrast, the "Dragon Bone" segment has little or no crust and no sign of hydrothermal activity has been found (Dick and Zhou, 2015; Zhou and Dick, 2013).

Most peridotites reported in this paper are from the western side of the Dragon Bone segment, and few samples are from the western side of the Gazelle transform fault (Fig. 1). The positions of all the samples recovered from this area are also indicated in Supplementary Data Fig. S1. Our samples were collected by dredging and television-guided (TV)-grabs (Table 1). Dredge D9 is located on the outside-corner high of the western ridge-transform intersection. TV-grab TVG10 is located on the eastern inside corner high. TV-grabs TVG3 and TVG4 are located at the northeast corner and close to the segment center, respectively, near the crest of the southern rift valley wall. These locations comprise the northern and southern of three domes in the southern rift mountains staggered progressively north and east from the Gallieni fracture zone (Zhou and Dick, 2013; Fig. 1). Further in the southern rift mountains, dredges D1, D4-2, D5 and D6 were recovered, among which dredges D5, D1, and D4-2 are located progressively southward along the segment end, while dredge D6 lies close to the segment center.

#### 3. Analytical methods

#### 3.1. Petrography and mineralogy

Identification of minerals and observation of the micro-structures were conducted on standard thin sections under a Leica DM4500P optical microscope at Tongji University. Major element compositions of the minerals (Spl, orthopyroxene and Cpx) and backscattered electron images were obtained with a JEOL JXA-8100 electron microprobe. Data were obtained on two electron microprobes of the same type using the same settings at the Guangzhou Institute of Geochemistry, Chinese Academy of Sciences. The reproducibility between the two instruments was within the absolute error. In-situ spot analyses of minerals were performed with a 2- $\mu$ m diameter electron beam at 15-kV acceleration voltage and 2  $\times$  10 $^{-8}$  A using SPI international standards and an absolute error <0.02 wt% (Reed, 2005). Backscattered electron images were captured at the China University of Geosciences, Wuhan.

# 3.2. In-situ trace element compositions

Cpx trace element compositions were determined by laser ablation inductively coupled plasma mass spectrometry (LA-ICP-MS). Peridotite fragments were crushed, and Cpx grains were handpicked under a binocular microscope and mounted in epoxy in holes in an aluminum disk. Sample surfaces were polished and analyzed by an Electro Scientific Instruments (ESI) New Wave UP193 FX excimer (193 nm) laser ablation system coupled to a Thermo Element XR Inductively Coupled Plasma-

**Table 1**Sample locations, depths, geologic settings of harzburgite on the Dragon Bone amagmatic segment.

Samples	Depth (mbsl)	Longitude (°E)	Latitude (°S)	Samples used in this study	Geologic settings	
Segment End						
21 V-TVG3	2806	52.50108	36.3258	TVG3-1, TVG3-5	Northwest corner	
21 V-D1	2045	52.55821	36.50597	D1-4, D1-6, D1-12, D1-13 <sup>a</sup>	Rift mountains	
21 V-D4-2	2388	52.51546	36.67474	D4-2-6/-7/-8/-9	Rift mountains	
21 V-D5	2040	52.572	36.44977	D5-1, D5-2	Rift mountains	
21 V-D9	3515	52.48846	36.03636	D9-1, D9-9 <sup>b</sup>	Outside corner	
21VII-TVG10	2661	53.2881	36.08682	TVG10-2, TVG10-3	Inside corner	
Segment Center						
21 V-TVG4	2089	52.8631	36.2212	TVG4-1/4-3/4-4/4-5	Domes	
21 V-D6	1524	52.73858	36.44227	D6-1, D6-5	Rift mountains	
EDUL D69 <sup>c</sup>	3850	52.993	36.1367	EDUL D69	Axial valley	
30-IV-D2 <sup>d</sup>	3577	52.8752	36.1063		Axial center	
21-V-D2 <sup>d</sup>	1789	52.7672	36.8034		Rift mountain	

a: Cpx-rich harzburgite; b: part of D9-9 was metasomatized by gabbroic veins; c: from Seyler et al. (2003, 2011); d: two basalt glasses in Fig. 1.

Mass Spectrometer (ICP-MS) at the Plasma Analytical Facility of the National High Magnetic Field Laboratory, Florida State University. The laser energy flux was 6-8 J/cm². Spot analyses were performed using  $100 \, \mu m$  spots at 50 Hz repetition rate and 20 s dwell time per spot, with USGS basalt standards BCR-2 g, BHVO-2 g, and BIR-1 g, and NIST SRM 610 (Jochum et al., 2015), Yang et al., 2015). Major elements determined by LA-ICP-MS have been shown to be comparable to EMPA data in precision and accuracy (Humayun et al., 2010).

#### 4. Results

# 4.1. Petrography results

# 4.1.1. Hand specimens and thin sections

Polished surfaces of typical peridotites are shown in Fig. 2. All Dragon Bone peridotites are heavily serpentinized harzburgites containing few fresh olivine grains. Peridotites from dredges D5 and D6 are severely altered and preserve few fresh Cpx grains. Peridotite TVG3–1 is plastically deformed and shows strong foliation (Fig. 3a). The few unaltered Cpx grains in TV-grab TVG3 were fragmented during brittle deformation. Most of the orthopyroxene (Opx) in peridotite TVG4–1 are elongated (Fig. 3c) indicating ductile deformation. Although TVG4–1 peridotite did not experience brittle deformation as TVG3–1 did, coarse-grained Cpx are rarely recognized in TVG4–1 or other peridotites from TVG4 (e.g. TVG4–3/–4/–5). Peridotite D1–13 has at most 5% modal Cpx, and can thus be referred to as a Cpx-rich harzburgite (Fig. 3b).

Peridotite D9–9 is approximately twenty centimeters long with a corner of the sample containing a gabbroic vein. This portion of the sample (Figs. 2, 3d) is called 'D9–9 meta' here. The sutured contact between the peridotite and the gabbro indicates chemical interaction between an intruding melt and the peridotite along its path and likely a short distance into the host peridotite as well. Opx in the vein shows high interference colors indicating Fe-enrichment (Fig. 3e, f). Cpx and Opx major element compositions are also high in Ti and Fe, consistent with melt metasomatism. Trace elements analyses of Cpx away from the gabbroic vein, however, show typical abyssal harzburgite signatures, and the major elements from LA-ICP-MS do not show high Ti or Fe concentrations.

#### 4.1.2. Micro-structures

The peridotite microfabrics range from porphyroclastic to protogranular texture, though often elements of both are found within a single thin section. The former texture has rounded or elongated medium to coarse-grained pyroxene augen (or porphyroclasts), often kink banded or bent, in a matrix of recrystallized olivine (Figs. 3a, c, 4b). The latter have interlocking pyroxene and olivine with smooth curved grain boundaries with deep embayments and little macroscopic evidence of deformation (Figs. 3a, d, 4a, c, d). The embayments are often interpreted as the products of pressure-solution or coble creep during mantle melting (Dick, 1977), and in other cases as evidence of late-stage melt impregnation (Menzies, 1973). While protogranular texture has been generally assumed to represent the earliest formed, it can also be found overprinting porphyroclastic textures. Differentiation between

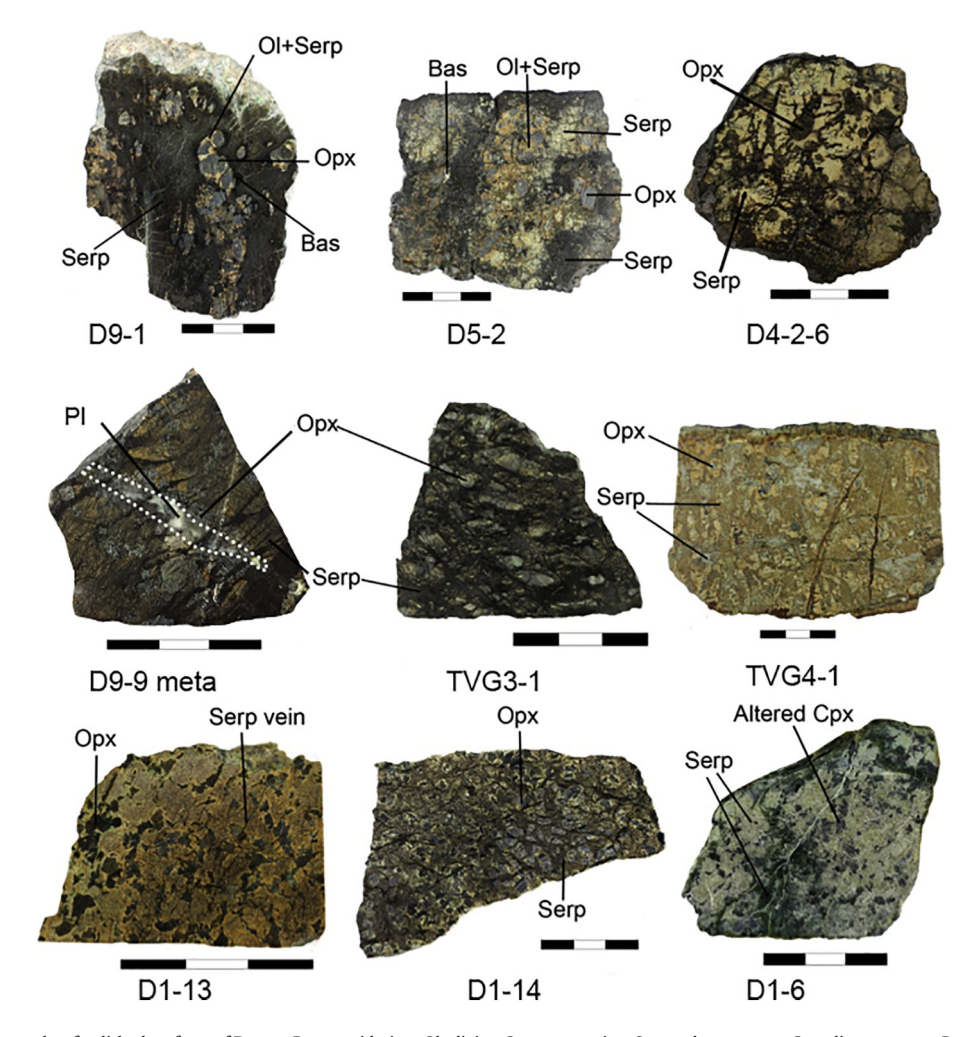


Fig. 2. Representative photographs of polished surfaces of Dragon Bone peridotites. Ol-olivine, Serp-serpentine, Opx-orthopyroxene, Cpx-clinopyroxene, Bas-bastite. Pl-plagioclase. D9–9 meta is a portion of a larger sample crosscut by a gabbroic vein with the white dotted lines showing its location.

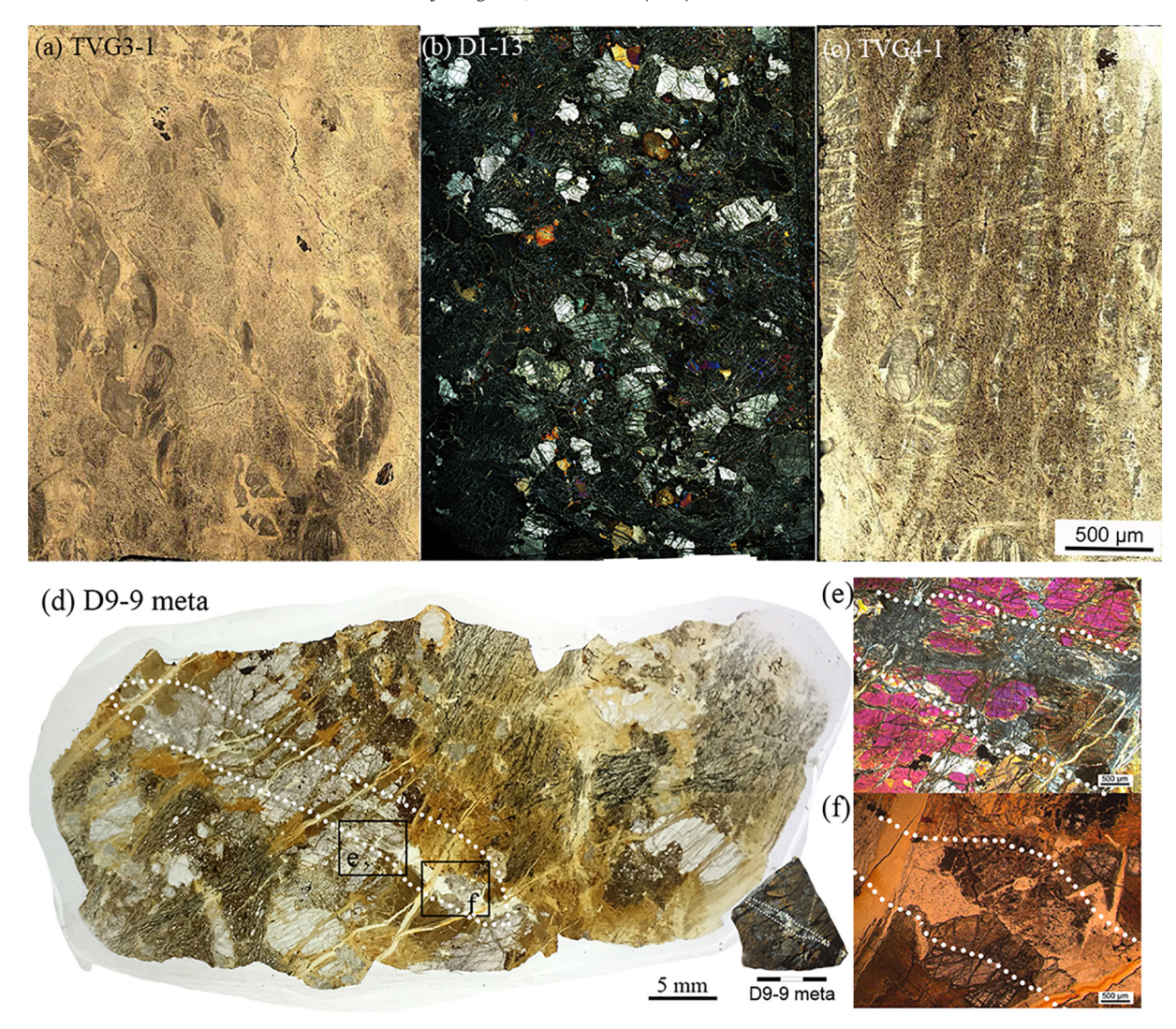


Fig. 3. Photomicrographs of Dragon Bone peridotites; (a) TVG3-1 in plane-polarized light (PPL) showing deformed foliation; (b) D1-13 in cross-polarized light (XPL) showing embayed Opx (white and grey colored) and Cpx grains (yellow and orange colored); (c) TVG4-1 (PPL) characterized by elongate stretched Opx grains; (d) D9-9 meta (PPL) with gabbro vein outlined by the white dotted line. Rectangles (e) and (f) are magnified on right (XPL).

these origins can be difficult, though in the case of melt impregnation elevated TiO<sub>2</sub> in spinel, and elevated Na<sub>2</sub>O in pyroxene, or the presence of plagioclase are generally definitive, as is a refractory composition for progressive partial melting (Dick and Bullen, 1984). In our samples most, and often all, the olivine is replaced by serpentine  $\pm$  magnetite. Elongated Opx grains with undulose extinction are found in TVG4-1 (Fig. 3c). In addition, plastically deformed Opx grains define a foliation in TVG 3-1 (Fig. 4b). Only a few Cpx relicts are retained in these samples, indicating a refractory composition. Convex grain rims typically characterize the fine- to coarse-grained Cpx grains. They also appear in the form of 'Cpx-Spl' aggregates within Opx embayments. Spinel often appears in holly-leaf (Fig. 4g) or vermiform shapes in symplectites (Fig. 4h, i). Some fine-grained spinel are observed in the olivine matrix and are interpreted as due to reactive crystallization (crystallization simultaneous with melt-rock reaction within the conductive thermal boundary layer, e.g. Collier and Kelemen, 2010) within the dissolution embayment of Cpx in D9-1 (Fig. 4j, k).

One of the most distinctive micro-structures in Dragon Bone peridotites is symplectite formed by the intergrowth of 'Cpx-Spl-Opx' at the expense of Opx. Coarse symplectites and Cpx and Opx with dissolution embayments are extensively developed in the Cpx-rich harzburgite D1–13 (Figs. 3b, 4a, c, d, and i). Symplectites in Dragon Bone peridotites

can be classified into two types: 'Spl-Cpx-Opx' type and 'Spl-Cpx' type. Most Dragon Bone peridotite symplectites form rims around convex Cpx, or are found in the Opx embayments (e.g., Fig. 4c, e, f), and some even appear to be 'drifting' away from the embayments (Fig. 5). Symplectitic structures in abyssal peridotites have also been reported at other places, such as the Hole 1274A peridotites from the slow spreading Mid-Atlantic Ridge (Seyler et al., 2007; Suhr et al., 2008). A coarse-grained Opx hosting a micron-scale veinlet in its rim shows a reactive impregnation forming an irregular 'Ol-Cpx-Spl' pocket in TVG4–1 (Fig. 4e, f).

# 4.2. Major elements mineral compositions

# 4.2.1. Spinel

Average spinel major element compositions are listed in Table 2. Individual spot analyses are reported in Supplementary Table S1. On a thin section scale, holly-leaf spinel shows limited compositional variation. For example, average holly-leaf spinel  $100^*\text{Cr}^{3+}/(\text{Cr}^{3+}+\text{Al}^{3+})$  (Cr#) in segment center peridotites (e.g., TVG4–1) is  $37.1 \pm 3.8$ . Spinel from segment-end peridotites has lower Cr# varying from 19.0 to 26.5 from near the ridge axis to off-axis (Fig. 6). Symplectitic spinel, which occurs extensively in D1–13, displays almost the entire range of composition of the Dragon Bone peridotites (Fig. 6). Symplectitic spinel Cr# in

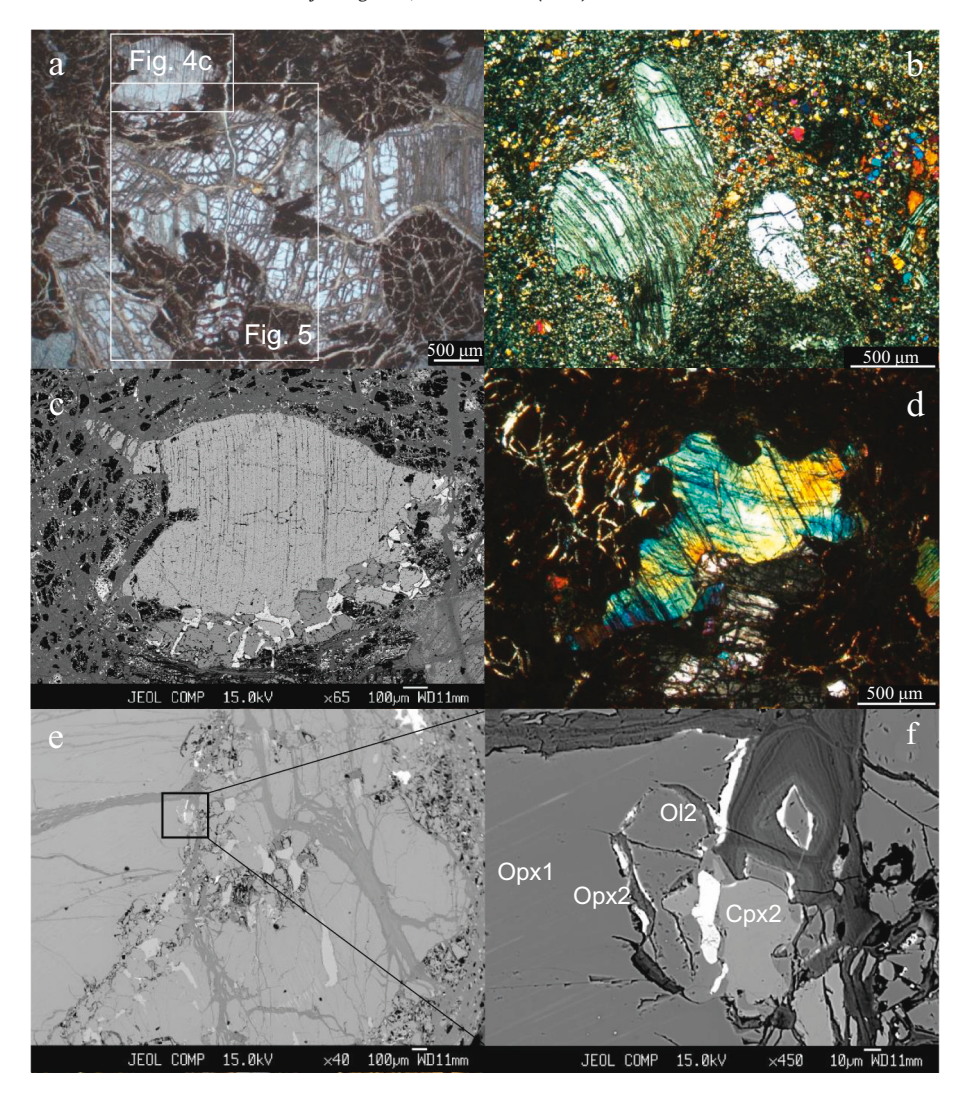


Fig. 4. Photomicrographs of Dragon Bone segment harzburgites: (a) Opx dissolution embayments in sample D1–13 (PPL); (b) Deformed Opx with undulose extinction in sample TVG3–1 (XPL); (c) Backscattered electron image of Cpx-spinel symplectite on the convex rim of Cpx in the upper inset in Fig. 4a; (d) Cpx dissolution embayments in sample D1–13 (PPL); (e) Opx porphyroclast: black rectangle outlines intergrown Ol, Cpx, and Spl in 4f; (f) Backscattered electron image of olivine (Ol 2) and clinopyroxene (Cpx 2) generated through reaction with orthopyroxene (Opx 1) and exotic melt; (g) Holly-leaf spinel in sample TVG4–1 in plane-polarized light; (h) Backscattered electron image of vermiform spinel in sample D9–1; (i) Vermiform spinel in sample D1–13 under cross-polarized light. (j) and (k) Backscattered electron images of reactive crystallized spinel grains in the olivine matrix in the Cpx embayments (sample D9–1).

D1–13 ranges from 26.0 to 42.8, while holly-leaf spinel has uniform Cr# of 24.3–26.2 (Fig. 6).

Peridotite D9–9 meta (Fig. 2 and Fig. 4) has only fresh Cpx and Opx and no spinel in thin section. Sample D9–1 (Fig. 4j, k) has fine-grained spinel in the olivine matrix in the Cpx embayment with Cr# of ~52.5 and high  $\rm TiO_2$  content (0.89 wt%) and plots along the olivine fractionation trend (Fig. 6). This kind of spinel is identified as the product of reactive crystallization during late-stage melt percolating reaction and is indicated as 'D9–1 reactive crx' in figures. Other symplectitic spinel from D9–1 peridotite has lower Cr# number (23.9) and lower  $\rm TiO_2$  content (0.05 wt%) (Fig. 6).

# 4.2.2. Orthopyroxene

Average in-situ major element Opx analyses are listed in Table 3. Individual spot analyses are reported in Supplementary Table S2. Most Opx porphyroclasts in Dragon Bone peridotites are primary. Apart from the dredge D9 peridotites, Opx  $100^* \text{Mg}^{2+}/(\text{Mg}^{2+}+\text{Fe}^{2+})$  (Mg#) has a narrow range (89.8–91.4). Opx from the gabbroic vein in sample D9–9 meta, however, has Mg# as low as 82.2 and TiO<sub>2</sub> up to 0.36 wt%. Detailed analyses show a gradient of higher FeO and TiO<sub>2</sub> in the host peridotite towards the gabbroic veins at a distance of about 1 cm.

# 4.2.3. Clinopyroxene

Major element compositions of Cpx are listed in Table 4, EPMA and LA-ICP-MS on individual spots are reported in Supplementary Table S3. Three main types of Cpx are identified: 1) primary Cpx, 2) Cpx in symplectites (specifically in D1-13), and 3) reactive crystallized Cpx in D9-1 and in a melt pocket in TVG4-1. Cpx from segment center peridotites has relatively higher Na<sub>2</sub>O than segment-end Cpx for a given TiO<sub>2</sub> content (Fig. 7). The segment-center and segmentend Cpx form separate trends. The exceptions are D1-13 and D1-6, segment end peridotites lying on the segment center trend, and D9-9 meta, which lies in the gabbro vein field. D1-6 Cpx has relatively high Na<sub>2</sub>O (0.39 wt%) while D1-13 has low Na<sub>2</sub>O (0.20 wt%). Cpx in D9-9 meta has variable TiO<sub>2</sub> (0.18-0.63 wt%) and high Na<sub>2</sub>O content due to metasomatism related to gabbro veins (Fig. 7). Cpx in samples D9-1 and D9-9 meta has higher Fe content than Cpx in other peridotites and has Mg# between 84.7 and 89.3 while Cpx Mg# in other samples ranges from 91.1–93.6. Fine-grained Cpx derived by reactive crystallization in D9-1 has significantly lower Na<sub>2</sub>O content (avg. 0.16 wt%) than other primary Cpx (avg. Na<sub>2</sub>O 0.33 wt%) as well as high Mg# (91.2) compared to other D9 Cpx.

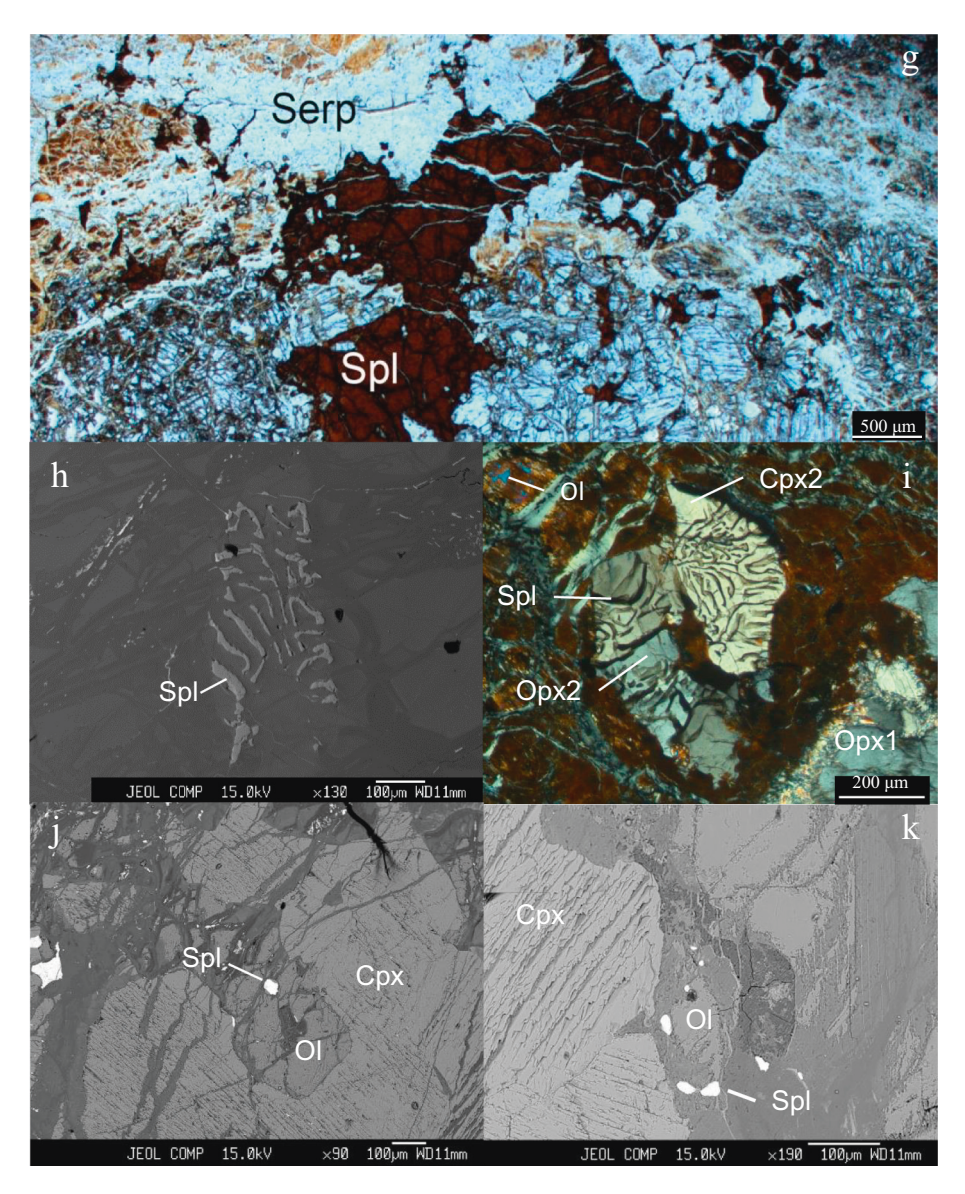


Fig. 4 (continued).

#### 4.3. Rare earth elements in pyroxene

# 4.3.1. Orthopyroxene

Opx trace element concentrations could be analyzed only in two segment-end peridotites D1–13 and D4–2-8 and a segment-center peridotite TVG4–4 (individual spot analyses are listed in Supplementary Table S4). D1–13 and D4–2-8 Opx are depleted in their rare earth element (REE) patterns (Supplementary Data Fig.S2). TVG4–4 Opx also shows a very steep depletion with the lowest heavy REE (HREE) abundances among these three samples; the light REE (LREE) of TVG4–4 Opx are higher than those of the other two samples (Supplementary Data Fig. S2).

#### 4.3.2. Clinopyroxene

Chondrite normalized REE patterns for individual spot analyses in Cpx are presented in Fig. 8. Individual spots analyses are reported in Supplementary Table S5. These patterns are also compared with calculated Cpx REE patterns after different degrees of partial melting of a depleted MORB mantle (DMM, Salters and Stracke, 2004) at 1.5 GPa.

The segment-end peridotite Cpx show variable LREE depletions in individual samples. These range from simple residual patterns, above

which there are patterns sequentially elevated in La, Ce and Nd. These are characteristic patterns predicted for varying amounts of partial chromatographic interaction with a migrating melt (Navon and Stolper, 1987). The extent of this effect ranges from little or none in samples D1–12 and D1–13, to considerable upward kicks in the LREE, with sample TVG10–3 showing the most extreme effect. Taken overall, the depleted patterns, based on the model source composition, indicate a range of approximately 7 to 13% melt removal, prior to modification by small fractions of migrating melt. By contrast the segment center peridotites show more complex patterns, with none retaining the pattern of a simple or only partially reacted residual compositions. Instead they have both elevated LREE and middle REE (MREE).

Three types of Dragon Bone peridotite Cpx are identified based on their sample locations and REE patterns. (1) Segment-end Cpx (dredges D1, D4–2, D5 and D9 and TV-grab TVG3) nearly all extend to depleted REE patterns with nearly flat HREE, mildly depleted MREE, and depleted LREE. (La/Ce)<sub>N</sub>, however, is >1 in nearly half the segment-end individual spot analyses. Both samples TVG3–1 and TVG3–5 have one analysis that shows significant Ce and Nd enrichments, but the rest of the LREE are depleted. Both spots are partly on an alteration patch and thus did not measure pristine Cpx. Although D9–9 is crosscut by a gabbroic vein,

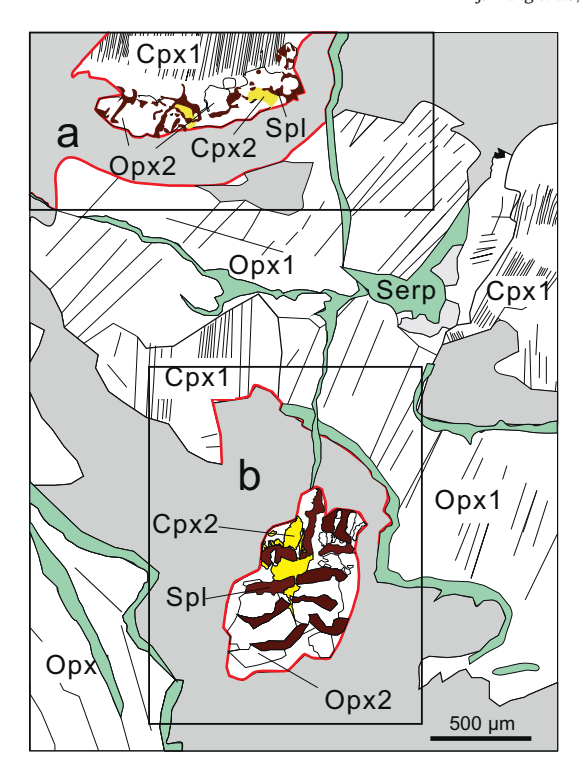


**Fig. 5.** Sketch illustration of symplectites near porphyroclastic Opx (D1–13). Red lines indicate where the original locations of symplectites should be. This figure is a magnified view of the large rectangle in Fig. 4a. Cpx-Spl aggregate (a) and Cpx2-Opx2-Spl aggregate (b) interpreted as due to breakdown of garnet as discussed in Section5.2.1.

most of the REE data for D9–9 obtained centimeters away from the gabbro vein do not show enrichment. Cpx from dredge D1 shows the most depleted REE patterns among the segment-end peridotites with LREE concentrations below the detection limit. These LREE-depleted segment-end Cpx also have the lowest trace element abundances, steepest LREE slopes and even lower HREE abundances than published SWIR peridotites from Seyler et al. (2011) (Supplementary Data Fig.

S3). (2) Several Cpx analyses from samples TVG10–3 and D9–9 show spoon-shaped REE patterns. Eight spots in five TVG10–3 Cpx grains (~1 mm width) at cores and rims were analyzed, and they are quite variable in LREE compositions. TVG10–3 Cpx has the highest HREE content of the Dragon Bone segment, indicating that it has seen limited amount of melt extraction. (3) Cpx from the segment-center (from D6 and TVG4) has the lowest HREE abundance, indicating the highest extent of partial melting among these Dragon Bone peridotites prior to later modification of the middle and light REE.

#### 5. Discussion

#### 5.1. Types of peridotites and melting processes

# 5.1.1. Melting mode (fractional or batch melting) and type of peridotites (residual or refertilized)

In this study, the Dragon Bone Cpx data are compared with published data along the SWIR to the east from 54° E to 68° E (Seyler et al., 2003) and to the west from 43° E to 46° E SWIR (Seyler and Brunelli, 2018). The Dragon Bone segment-end Cpx (except for D9–1 and D1–6 Cpx) overlaps in composition with Cpx between 54° E and 60° E (Fig. 9), plotting within the field of abyssal residual peridotites globally (Warren, 2016). Dragon Bone segment-center Cpx grains as well as Cpx from some peridotites previously dredged from the Dragon Bone spreading center during the EDUL cruise (i.e., EDUL D69 at 52.993°E SWIR, Fig. 1) display high Cr# with slightly higher Na contents than those from the segment-end Cpx (Fig. 9).

A comparison of the non-modal melting paths by Seyler and Brunelli (2018) with the Dragon Bone data suggests that the segment-end Cpx (except for D9–1 and D1–6) can be formed by near fractional melting of DMM with Na partition coefficient between Cpx and melt  $(D_{\rm N}^{\rm Cpx/l})$  equal to 0.30 corresponding to a melting pressure of 2 GPa according to Longhi (2002) (Fig. 9). This fractional melting trend at  $D_{\rm N}^{\rm Cpx/l}=0.30$  is also a better fit than batch melting for the general trend formed by abyssal residual peridotites (Fig. 9a). Although the Na-Cr# covariations of segment-end Cpx can be also modeled by near batch melting with a lower  $D_{\rm N}^{\rm Cpx/l}$  according to Seyler and Brunelli (2018), their REE patterns, however, indicate near-fractional melting.

The Dragon Bone segment-center Cpx as well as EDUL D69 can be modeled by near batch melting with  $D_{\rm Na}^{\rm Cpx/l}=0.30$  (Fig. 9a). However,

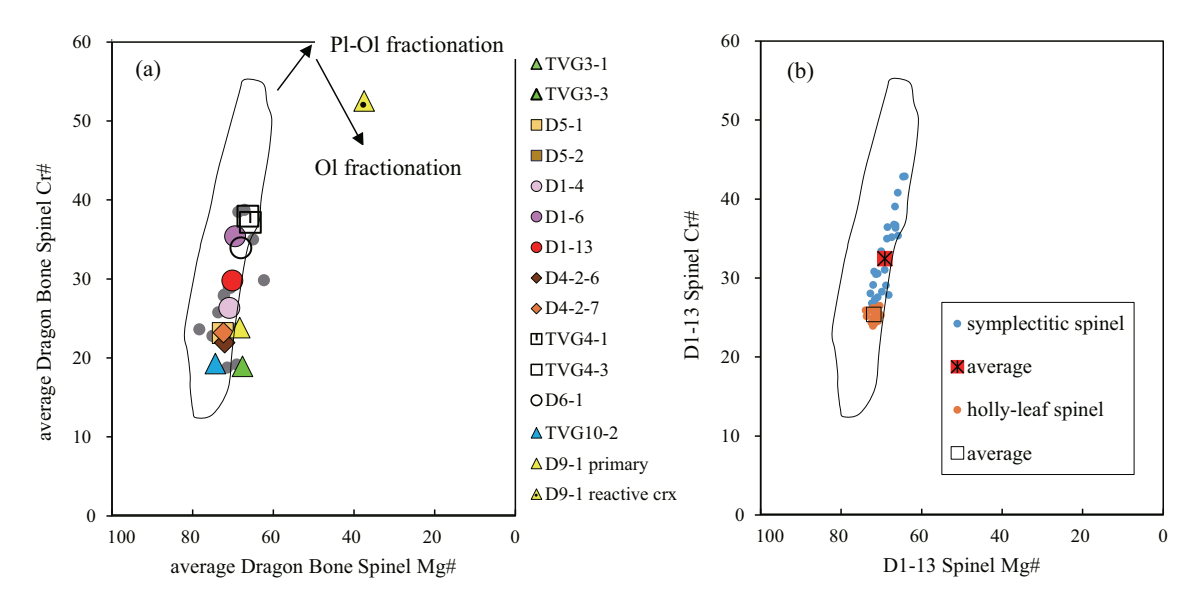


Fig. 6. (a) Representative spinel Cr# versus Mg# of Dragon Bone peridotites;  $Cr# = 100^*Cr^{3+}/(Cr^{3+}/Al^{3+})$ ,  $Mg# = 100^*Mg^{2+}/(Mg^{2+}+Fe^{2+})$ . Plotted are the sample averages of spot analyses of spinels. Grey points are Dragon Bone spinel data derived from Zhou and Dick (2013). 'D9-1 reactive crx' indicates reactive crystallized Cpx in D9-1. Primary Cpx in D9-1 is named as 'D9-1 primary'. Outlined is the compositional range of abyssal peridotite spinel compositions globally and the two black lines with arrows showing the trends of plagioclase-olivine (Pl-Ol) fractionation and Ol fractionation are after Dick and Bullen (1984). (b) Spinel Cr# versus Mg# of individual spot analyses of spinel in D1-13 peridotite.

**Table 2**Average major elements compositions of spinels in Dragon Bone peridotites (wt%).

Spinel	No.	SiO <sub>2</sub>	TiO <sub>2</sub>	Al <sub>2</sub> O <sub>3</sub>	Cr <sub>2</sub> O <sub>3</sub>	FeO	MnO	MgO	NiO	Total	Mg#	Cr#
New JEOL JXA-8100	)											
21-7-TVG10-2	4	0.07	0.01	50.28	17.90	11.48	0.13	18.74	0.33	99.05	74.4	19.3
21-5-TVG4-3	4	0.03	0.01	36.76	33.46	13.81	0.20	15.25	0.15	99.71	66.3	37.9
21-5-TVG3-3	3	0.01	0.02	50.40	17.58	14.40	0.14	16.91	0.30	99.76	67.7	19.0
21-5-D5-1	5	0.02	0.02	47.82	21.48	12.14	0.16	17.99	0.28	99.91	72.5	23.2
Old JEOL JXA-8100												
21-5-TVG3-1	5	0.02	0.05	49.46	17.30	15.06	0.13	16.46	0.25	98.79	67.5	19.0
21-5-D5-2	1	0.05	0.08	47.59	20.51	12.41	0.13	17.77	0.26	98.81	72.8	22.4
21-5-D1-4	2	0.02	0.04	45.13	24.03	13.21	0.15	17.29	0.21	100.12	70.9	26.3
21-5-D1-6	4	0.02	0.09	38.56	31.47	13.48	0.20	16.49	0.16	100.51	69.5	35.4
21-5-D1-13 <sup>a</sup>	17	0.03	0.01	46.13	23.40	12.62	0.14	17.63	0.20	100.21	71.9	25.4
21-5-D1-13 <sup>b</sup>	28	0.09	0.03	40.66	28.98	13.48	0.17	16.52	0.17	100.15	69.2	32.4
21-5-D4-2-6	6	0.01	0.06	48.85	20.45	12.63	0.11	17.90	0.25	100.29	72.1	21.9
21-5-D4-2-7	15	0.02	0.05	47.93	21.61	12.72	0.14	17.97	0.23	100.74	72.4	23.2
21-5-D6-1	10	0.04	0.05	39.53	30.24	14.26	0.18	16.23	0.17	100.72	68.0	33.9
21-5-TVG4-1	16	0.04	0.04	36.78	32.32	15.31	0.19	15.37	0.14	100.30	65.7	37.1
21-5-D9-1 <sup>c</sup>	11	0.10	0.89	23.24	38.20	28.43	0.36	7.83	0.12	99.22	37.5	52.5
21-5-D9-1 <sup>b</sup>	1	0.04	0.05	46.97	21.93	14.48	0.13	16.79	0.23	100.66	68.4	23.9

a: holly-leaf spinel, b: symplectitic spinel, c: reactive crystallized spinel.

their strong preferential enrichment in LREE and MREE excludes a pure depletion history although their HREE abundances are low. Hence, segment-center peridotites cannot be interpreted as simple residues of either batch or fractional melting.

Cpx Na<sub>2</sub>O and TiO<sub>2</sub> contents are commonly used to identify the degree to which a sample can represent a simple residue of melting or the extent to which it has been impregnated by an exotic melt (e.g., Dick, 1989; Dijkstra et al., 2003; Hellebrand et al., 2002; Hellebrand and Snow, 2003). Na<sub>2</sub>O contents of most Dragon Bone segment-end Cpx plot within the range of residues of fractional melting of Cpx derived from a DMM (Salters and Stracke, 2004) at a pressure of about 2.0 GPa with  $D_{Na}^{\text{Cpx/I}} = 0.30$  (Longhi, 2002), suggesting that these peridotites are simple residues (Fig. 9b). Exceptions in segment-end Cpx are from dredges D1 and D9. The spinel Cr# of D1–6 was measured on a symplectitic spinel relict which may not reflect the virtual degree of melting of D1–6. Na<sub>2</sub>O and TiO<sub>2</sub> covariations from individual spot data of D1–6 Cpx show similar negative trend to D1–13 Cpx (Supplementary Data Fig. S4) and a discussion on this phenomenon is given in Section 5.2.1 and in the supplementary material. Cpx from peridotite

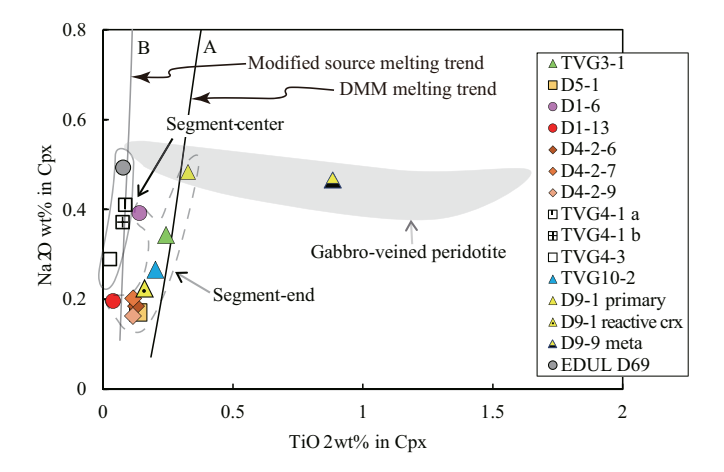


**Fig. 7.** Plot of Cpx  $TiO_2$  versus  $Na_2O$  content for average individual sample spot compositions. Average of EDUL cruise dredge D69 peridotites from 52.993° E SWIR (Seyler et al., 2011) are shown for comparison. Lines A and B are taken from Seyler et al. (2003). Line A: polybaric fractional melting of Cpx from a depleted MORB mantle source. Line B: polybaric fractional melting of a Cpx from a source modified by melt extraction and possible metasomatism. For parameters used for the melting model see Seyler et al. (2003). Melting begins at 2 GPa. The grey area is the composition range of Cpx in gabbro-veined peridotite D9–9 meta.

D9–1 has high  $Na_2O$  content although the modal composition does not show enrichment. In addition, the D9–1 spinel has slightly higher  $TiO_2$  content (> 0.12 wt%), which indicates that D9–1 could have suffered minor melt impregnation (Dick, 1989; Dick and Bullen, 1984; Mallick et al., 2014). The gabbro-vein influenced Cpx in D9–9 meta has a variable  $TiO_2$  content (Fig. 7). The reactive crystallized Cpx in D9–1 does not have high  $TiO_2$  content and most REE patterns of D9–9 away from the gabbro-vein are typical for simple residues of fractional melting (Fig. 8).

Segment-center Cpx deviates from the residue trajectory of low-pressure fractional melting but still lies in the abyssal peridotite field (Fig. 9b), indicating that these peridotites likely have suffered Nametasomatism or melted at a higher pressure. As shown in Fig. 9b, the latter case requires fractional melting with  $D_{\rm Na}^{\rm Cpx/l}$  near 0.70.  $D_{\rm Na}^{\rm Cpx/l}$  (0.70) is the highest experimental value measured at 3 GPa, while the average  $D_{\rm Na}^{\rm Cpx/l}$  at 3 GPa is 0.46 (Longhi, 2002). To explain the high Na contents of segment-center Cpx by melting, a pressure of 3 GPa or higher is required. This would place the onset of melting in the garnet stability field (Bédard, 2014; Longhi, 2002; Seyler and Brunelli, 2018). In contrast, HREE of the segment-center Cpx does not record any high degrees of melting in the garnet stability field. Hence, Nametasomatism similar to that proposed by Seyler et al. (2003) is a likely process to have caused the Na-enrichment and is also consistent with the elevated LREE and MREE compared to HREE in segment-center Cpx.

# 5.1.2. Two-stage depletions

On a TiO<sub>2</sub> versus Na<sub>2</sub>O plot the segment-center Cpx forms a trend separate from most segment-end Cpx (Fig. 7). Segment-center Cpx are distributed along line B which was interpreted by Seyler et al. (2003) as melting residues from a metasomatized extraction-modified mantle. Those Cpx compositions are characterized by higher Na<sub>2</sub>O and lower TiO<sub>2</sub> contents than the segment-end Cpx that forms the line A - residual Cpx of a DMM (Seyler et al., 2003). The high Na content of the segmentcenter Cpx could be explained by an initial depletion, followed by metasomatism. This will be discussed in Section 5.2.3. An alternative explanation for the segment center trend is to first deplete the peridotite at higher pressure where more Na is retained in the pyroxene, and a subsequent depletion at lower pressure.  $D_{Na}^{Cpx/l}$  is pressure dependent; for a given degree of melting, a higher-pressure residue will retain more Na than at lower pressure (Longhi, 2002). In this two-stage depletion, Ti is depleted during the higher-pressure event, but Na is not, while the second depletion event at lower pressure beneath the modern ridge axis depletes both Na and Ti. The two-stage depletion is also consistent with the segment-end peridotites as the rift mountains have large areas

**Table 3**Average major elements compositions of orthopyroxenes in Dragon Bone peridotites (wt%).

Орх	No.	SiO <sub>2</sub>	TiO <sub>2</sub>	Al <sub>2</sub> O <sub>3</sub>	Cr <sub>2</sub> O <sub>3</sub>	FeO	MnO	MgO	NiO	CaO	Na <sub>2</sub> O	Total	Mg#	Cr#
New JEOL JXA-8100														
21-7-T10-2	4	54.85	0.10	3.80	0.56	6.85	0.15	31.55	0.10	1.41	0.02	99.39	89.2	9.2
21-5-T4-3	2	55.27	0.01	2.98	0.84	5.77	0.11	31.89	0.10	2.32	0.03	99.32	90.9	15.7
21-5-D9-9 meta	19	54.18	0.36	2.15	0.40	11.32	0.26	29.00	0.07	1.66	0.03	99.42	82.2	10.1
21-5-T3-3	3	54.15	0.07	4.73	0.73	6.29	0.12	30.75	0.09	2.34	0.03	99.30	89.8	9.4
21-5-D5-1	3	54.21	0.07	4.57	0.83	6.34	0.14	31.10	0.10	2.10	0.00	99.46	89.8	10.8
21-5-D4-2-9	2	54.85	0.04	4.07	0.75	6.17	0.13	31.86	0.10	1.54	0.03	99.54	90.3	11.0
Old JEOL JXA-8100														
21-5-TVG3-1	5	54.36	0.05	4.95	0.72	6.22	0.14	31.11	0.10	1.32	0.02	99.02	89.9	8.9
21-5-TVG3-5	6	54.39	0.03	5.35	0.79	6.17	0.14	31.33	0.09	1.23	0.02	99.55	90.0	9.0
21-5-D5-2	6	54.59	0.07	4.84	0.90	5.93	0.13	31.01	0.07	1.85	0.03	99.43	90.3	11.1
21-5-D1-4	3	55.47	0.02	3.83	0.73	5.82	0.09	31.95	0.08	1.69	0.02	99.71	90.7	11.3
21-5-D1-13	28	55.38	0.02	3.41	0.78	5.84	0.14	32.21	0.08	1.12	0.01	99.00	90.8	13.3
21-5-D4-2-6	11	53.98	0.06	5.15	0.90	6.29	0.14	30.92	0.07	1.60	0.03	99.16	89.8	10.5
21-5-D4-2-7	8	54.67	0.05	4.63	0.86	5.78	0.14	31.74	0.09	1.41	0.02	99.41	90.7	11.0
21-5-TVG4-1	24	55.59	0.03	3.00	0.88	5.53	0.13	33.13	0.08	1.34	0.03	99.73	91.4	16.3
21-5-D9-1	30	54.33	0.12	3.74	0.77	8.22	0.19	30.22	0.07	1.39	0.03	99.08	86.8	12.4

of exposed peridotites and little or no basalt. The scarcity of basalt at the ridge axis indicates that a limited amount of melt was produced in the recent melting event. Thus, the recent melting event was minor, and the sub-ridge mantle was already more depleted than a normal MORB source (Zhou and Dick, 2013).

# 5.2. Refertilization

# 5.2.1. Identification of refertilization

Chen et al. (2015) suggest that a large volume of melt is trapped in the peridotites based on whole rock analyses of the peridotites; however, there is little evidence for this in the composition of the relict minerals. Near-fractional melting with efficient melt extraction depletes the residual peridotites in incompatible elements even at relatively low degrees of melting (e.g., Johnson et al., 1990). However, melt extraction is not always efficient and many peridotites are not simple residues but have undergone different degrees of refertilization due to inefficient melt extraction at the end of mantle melting as the lithosphere-asthenosphere boundary is approached (e.g., Brunelli et al., 2006; Dick et al., 1984; Hellebrand et al., 2002; Warren and Shimizu, 2010).

To further examine the extent to which the Dragon Bone peridotites were refertilized, we modeled the depletion and refertilization for Ti versus Zr abundances starting from a depleted mantle source composition (Salters and Stracke, 2004). The modeling indicates that the segment-end Cpx grains, except that from sample D1–13, plot along a depletion trend for fractional melting with a residual porosity between 0 and 0.5% (Fig. 11). Cpx from D1–13, the Cpx-rich harzburgite that is

characterized by extensively developed dissolution embayments and symplectites, plots off the depletion trend. Its Zr concentration is at the detection limit of approximately 50 ppb, which is the likely cause for the deviation from the trend. D1–13 Cpx has the most depleted Dragon Bone peridotite REE patterns (Fig. 8), its Na<sub>2</sub>O content falls in the field for residual abyssal peridotites (Fig. 9), and its spinel TiO<sub>2</sub> content is below 0.12 wt%. None of these characteristics indicate refertilization by anything resembling a MORB-like melt. The negative correlation of Na and Ti of individual analyses of D1–13 symplectitic Cpx is inconsistent with melt-rock reaction or refertilization by our modeled melt compositions (see supplementary material for more information). The symplectites in D1–13 most likely represent breakdown of garnet (Field and Haggerty, 1994; Shimizu et al., 2008) rather than product of melt-rock reaction (e.g., Seyler et al., 2007; Suhr et al., 2008; Warren, 2016).

By contrast to the remaining segment end peridotites, the segment center peridotites D6, TVG4, and EDUL D69 Cpx, all with high (Sm/Yb)  $_{\rm N}$  ratios, plot off the melt depletion trend and thus show evidence for significant local melt refertilization of the residual mantle.

# 5.2.2. Segment-end peridotites

The segment-end Cpx REE patterns all extend to strongly LREE depleted patterns, consistent with residues of fractional melting (Johnson et al., 1990). None of the peridotites contains plagioclase, nor do the REE patterns have Eu anomalies, and all have low TiO<sub>2</sub> contents. The segment-end peridotites show no obvious deviation from the Ti-Zr partial melting trend with porosity near 0.5% (Fig. 11), indicating that

**Table 4**Average major elements compositions of clinopyroxenes in Dragon Bone peridotites (wt%).

Срх	No.	SiO <sub>2</sub>	TiO <sub>2</sub>	Al <sub>2</sub> O <sub>3</sub>	Cr <sub>2</sub> O <sub>3</sub>	FeO	MnO	MgO	NiO	CaO	Na <sub>2</sub> O	Total	Mg#	Cr#
New JEOL JXA-8100														
21-5-D4-2-9	7	51.79	0.11	5.11	1.16	3.31	0.08	17.43	0.05	21.11	0.16	100.32	90.4	13.2
21-5-D5-1	7	50.97	0.14	5.47	1.25	3.15	0.10	16.58	0.05	22.11	0.17	99.99	90.4	13.3
21-5-TVG4-3	11	52.89	0.03	3.19	1.02	2.32	0.07	16.86	0.05	23.57	0.29	100.28	92.9	17.5
21-7-TVG10-2	7	51.10	0.20	5.37	1.02	2.76	0.09	16.39	0.05	22.72	0.27	99.96	91.4	11.4
21-5-D9-9 meta	8	50.90	0.88	3.88	0.84	4.44	0.14	15.56	0.04	22.44	0.46	99.59	86.3	12.1
Old JEOL JXA-8100														
21-5-TVG3-1	3	50.21	0.24	6.83	1.25	1.99	0.10	14.48	0.06	24.09	0.34	99.59	92.9	10.9
21-5-D1-6	4	51.91	0.14	4.02	1.33	2.23	0.09	16.05	0.04	23.21	0.39	99.42	92.8	18.1
21-5-D1-13	33	51.84	0.04	4.71	1.24	2.53	0.09	16.73	0.04	22.10	0.20	99.52	92.2	15.1
21-5-D4-2-6	26	50.78	0.13	5.78	1.27	2.80	0.10	16.11	0.05	22.06	0.19	99.27	91.1	12.9
21-5-D4-2-7	8	50.68	0.12	5.87	1.32	2.62	0.09	15.95	0.07	22.36	0.20	99.28	91.6	13.1
21-5-TVG4-1	38	52.30	0.09	3.45	1.30	2.03	0.08	16.64	0.04	22.81	0.41	99.14	93.6	20.0
21-5-D9-1 <sup>a</sup>	15	52.06	0.33	3.44	1.14	3.88	0.13	15.87	0.05	21.95	0.48	99.34	88.0	18.3
21-5-D9-1 <sup>b</sup>	4	50.72	0.16	5.17	1.24	2.70	0.07	15.74	0.07	22.61	0.22	98.71	91.2	13.9

a: primary Cpx, b: reactive recrystallized Cpx.

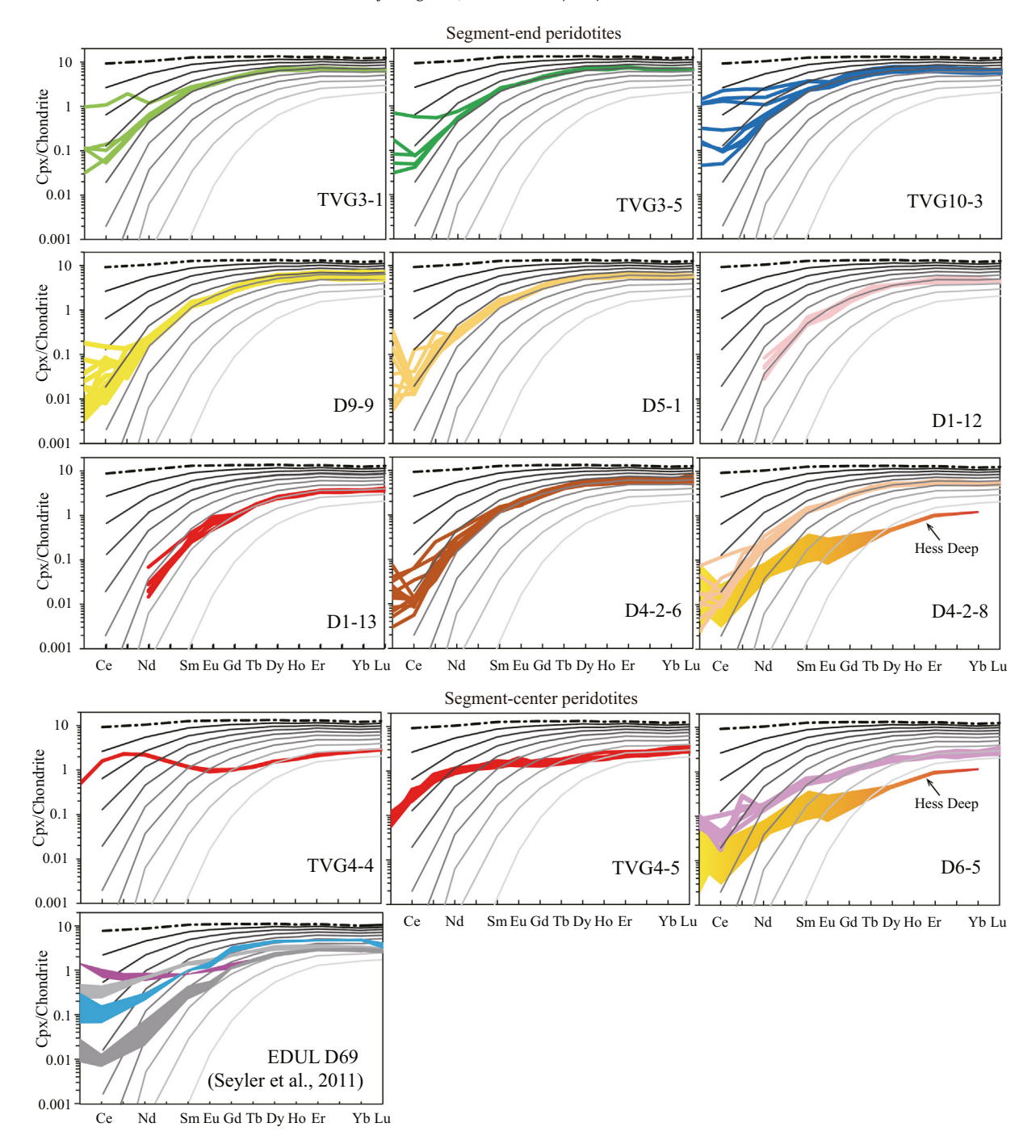


Fig. 8. Chondrite normalized REE patterns of Dragon Bone peridotites Cpx. Chondritic values from Anders and Grevesse (1989). Patterns are organized according to their geological setting and are compared to REE patterns of non-modal fractional melting of a depleted MORB mantle (DMM, Salters and Stracke, 2004). Four different REE patterns of Cpx from EDUL cruise dredge D69 peridotites (Seyler et al., 2011) are shown for comparison in the last panel. Dashed line represents Cpx composition of the depleted mantle in each panel. Solid lines are Cpx compositions in residues after successive 2% melting increments. The yellow field shows the refractory Hess Deep Cpx composition range from Dick and Natland (1996). Mineral-melt partition coefficients are after a compilation of Salters and Longhi (1999), Salters et al. (2002) and Sun and Liang (2012) with Cpx partition coefficients from 1.5 GPa and the melting reaction 0.560px + 0.72Cpx + 0.04Spl = 0.34Ol + 1melt (Longhi, 2002; Wasylenki et al., 2003) (Supplementary Table S6).

the amount of melt trapped in the mantle is very limited and that the peridotites are predominantly residual. The upward spread in LREE for individual peridotites, as discussed later, indicates only a partial chromatographic exchange, and thus that a very small volume of late melt has passed through the samples without significant melt retention. Our interpretation, then, is opposite to the conclusions of Chen et al. (2015) based on their study of bulk rock compositions. This study shows that the bulk rock composition of these highly serpentinized peridotites is altered including elements that are considered nominally

fluid-immobile or at low concentration in seawater (Frisby et al., 2016a, 2016b).

Several analyses from peridotite TVG10–3 Cpx show spoon-shaped patterns with increases in La, Ce and perhaps Nd and relatively uniform HREE contents. While most of D9–9 Cpx grains are LREE-depleted, several analyses in this sample exhibit slight elevation in La, Ce and Pr. This type of pattern is observed in metasomatized peridotites (Bodinier et al., 1990; Suhr et al., 1998) and, as stated above, are often attributed to chromatographic fractionation(e.g., Hellebrand et al., 2002; Johnson and Dick,

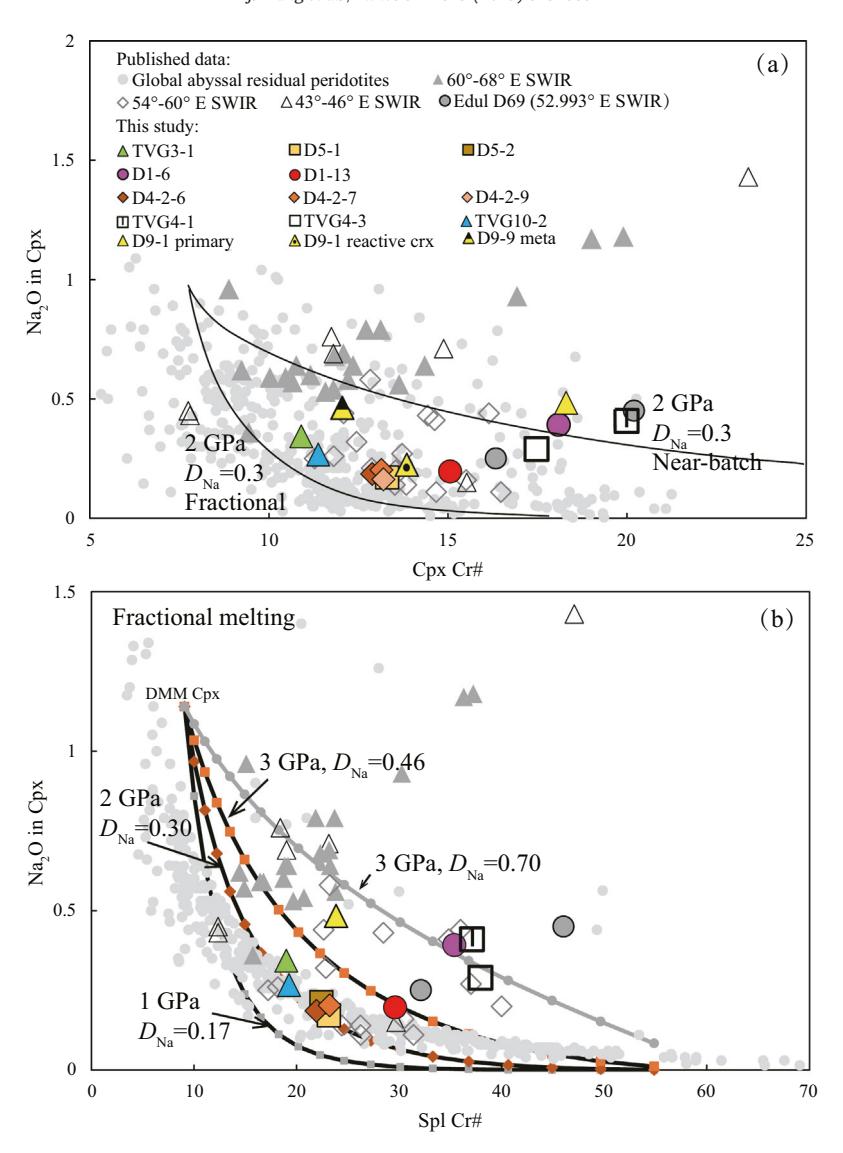


Fig. 9. (a) Covariations of Cpx Na<sub>2</sub>O content and Cr#. Data plotted are averages of spot analyses. Representive Cpx compositions from EDUL D69 from Dragon Bone segment (Seyler et al., 2003), from east of Melville fracture zone on the SWIR axis ( $60^{\circ}$ - $68^{\circ}$ E SWIR), from between Gazelle-Melville fracture zones ( $54^{\circ}$ - $60^{\circ}$ E SWIR) (Seyler et al., 2003) and the  $43^{\circ}$ - $46^{\circ}$ E SWIR segment (Seyler and Brunelli, 2018) are plotted for comparison. Grey circles in the background represent a compilation of residual abyssal peridotites (Warren, 2016). Two non-modal melting paths are shown: upper curve represents near-batch melting with residual mass porosity over amount of melting at each step of 0.6 with  $D_{Na}^{Cpx/l} = 0.3$  at about 2 GPa, and the lower curve represents fractional melting (see also Fig. 11a, b of Seyler and Brunelli, 2018). (b) Covariation of Cpx Na<sub>2</sub>O and associated spinel Cr#. Data plotted represent averages of spot analyses of clinopyroxene and spinel. Curves represent the fractional melting trends of DMM clinopyroxene (Salters and Stracke, 2004) in the spinel stability field with Na partition coefficient from Longhi (2002) at pressures of 1, 2, and 3 GPa.  $D_{Na}^{Cpx/l} = 0.46$  and 0.7 from Longhi (2002) are used for the two 3 GPa melting curves respectively. Hatch marks on curves indicate 1% melt increments.

1992; Navon and Stolper, 1987; Seyler et al., 2011) with LREEs progressively elevated to a larger extent than HREEs closer to melt transport channels. For TVG10-3 this transition from residual Cpx cores to metasomatized rims occurs on a length scale <2 mm. Similar incomplete homogenization of REE abundances in one single Cpx grain from core to rim has been found at the Atlantis Bank, from two peridotites located near the ridge axis (Warren and Shimizu, 2010). Warren and Shimizu (2010) calculated the time needed for trace element diffusive equilibration and found that such equilibration should be achieved in a short time (e.g. < 1 Myr) for <2 cm length scales of trace element variations at mantle temperatures. Accordingly, the trace element variations observed on a length scale of <2 mm\ in TVG10-3 should have achieved equilibration in an even shorter time. A likely explanation is that the degree of metasomatism was minimal, the temperature at which most melt-rock reactions took place was relatively low, and diffusion is too slow to achieve equilibrium. In addition, the low spinel TiO<sub>2</sub> content (<0.12 wt %) and the Cpx Ti–Zr covariation plotting along the pure partial melting

depletion trend suggest that TVG10–3 is very close to a pure mantle residue and that the sample has sustained minimal refertilization.

#### *5.2.3.* Segment-center peridotites

Dredge D6 and TV-grab TVG4 are located at the segment-center, and the Cpx REE patterns are unusually elevated in LREEs and MREEs, but are clearly depleted in HREEs (Lu to Tb). Such low HREE contents requires in excess of 14% melting of a depleted mantle source which is supported by the spinel Cr#. Similar Cpx REE patterns with low HREE abundances have been found in highly refractory peridotites (>18% melting) at the fast spreading Hess Deep (Dick and Natland, 1996), and we interpret the depleted HREE contents of the Cpx in the Dragon Bone peridotites to reflect a high extent of partial melting.

Their Cpx REE patterns do not fit simple partial melting models (Fig. 8). The convex REE patterns of TVG4 and D6 have also been found in other Cpx (Warren, 2016) and have often been argued to be

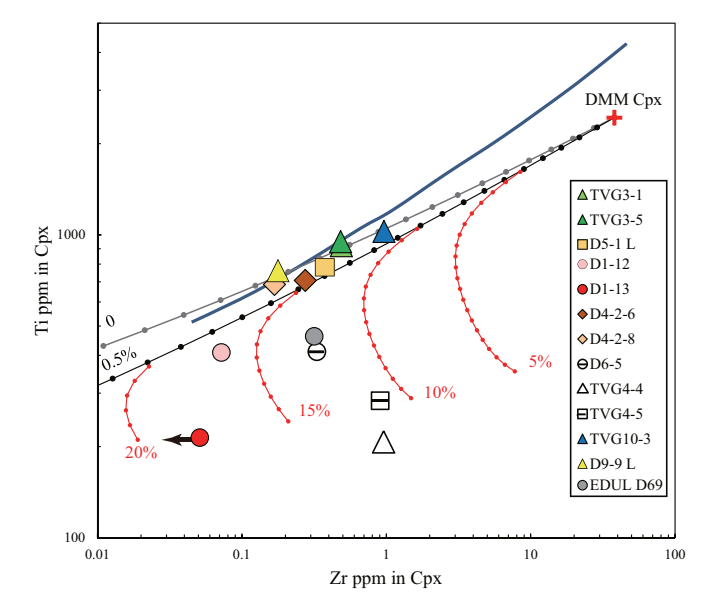


**Fig. 10.** Cpx Ti versus Zr average analyses for Dragon Bone peridotites. Grey dotted line shows the depletion trend for pure fractional melting in the spinel stability field for a DMM source (Salters and Stracke, 2004) with 1% melt increments, following the rational of Brunelli et al. (2006). Black dotted line is the depletion trend at 0.5% residual porosity. Red dotted curves represent variably depleted residual clinopyroxenes refertilized with an instantaneous melt extracted after 5%, 10%, 15% and 20% fractional melting of a DMM source. Partition coefficients are from Longhi (2002) and Salters et al. (2002). Spinel peridotite modes after Johnson (1998) and garnet peridotite modes are calculated from the spinel peridotite modal abundances using equations from Johnson et al. (1990). Melt modes in the garnet stability field are from Walter (1998) and melt modes in the spinel stability from Wasylenki et al. (2003). For comparison, the blue line is a similar depletion trend as modeled by Mallick et al. (2014).

due to refertilization by a low volume of enriched diffuse, non-channelized intergranular melts (Brunelli et al., 2006; Seyler et al., 2001, 2004, 2007; Warren, 2016; Warren and Shimizu, 2010). Both the Ti–Zr variations (Fig. 10) and the (Sm/Yb)<sub>N</sub> versus Yb<sub>N</sub> variations of the segment-center peridotites (Fig. 11) plotting off the partial melting trends of a depleted mantle indicate that pure partial melting cannot

account for the variations in D6 and TVG4 Cpx, but they require refertilization of a depleted residue.

This is also confirmed by petrographic evidence; for example in TVG4-1, a micron-scale irregular 'Ol-Cpx- Spl' pocket hosted by a coarse-grained Opx (Fig. 4e, f) is likely due to reactive impregnation suggesting entrapment of melt. In an ultraslow spreading setting, melt extraction rates are expected to be low (Brunelli et al., 2006; Chen et al., 2015; Seyler et al., 2011), increasing the likelihood for the entrapment of melt in the residual peridotites. During melt entrapment Cpx Cr# decreases or remains nearly constant while the Na<sub>2</sub>O content increases (Seyler and Brunelli, 2018). However, Na<sub>2</sub>O (0.27–0.54 wt%) and Cr# (15-23) variations of the fine-grained Cpx in Ol-Cpx-Spl pockets and other coarse-grained Cpx (e.g., in TVG4-1) show a positive correlation on a sample scale, while Cr# covers a large range. In addition, the fine-grained Cpx in the Ol-Cpx-Spl pockets and other coarser Cpx show similar ranges in composition. Thus, the entrapment of melt cannot explain the large and concomitant variations in Na<sub>2</sub>O and Cr#.

Trace elements of Cpx in segment-center peridotites show little variation on a sample scale. Their LREE and MREE contents are less depleted than expected from simple melting models. Samples TVG4–5 and D6–5 even show depleted patterns. For sample TVG4–5, although the MREEs are enriched compared to simple melting models, the REE pattern still shows depletions of La and Ce compared to Nd and Sm and is similar to sample EDUL D6–1–2 (Brunelli et al., 2014; Seyler et al., 2011) dredged elsewhere on the SW Indian Ridge. Temperature estimates based on the REE-in-two-pyroxenes thermometer (Liang et al., 2013) of sampleTVG4–4, the only segment-center sample with both Opx and Cpx data, are 1205  $\pm$  38 °C at 1.2 GPa. This temperature estimate is similar to the temperature range obtained by (Seyler and Brunelli, 2018) on peridotites that sustained syn-melting metasomatism, and suggests that these variations are unaffected by post-melting metasomatism.

The high degree of depletion of the Dragon Bone mantle combined with the limited crustal thickness indicates that the mantle at the segment center also underwent two stages of depletion. The unusual REE patterns in the segment center peridotites can be explained in light of an ancient melting event that left a residue that was the product of 1% melting in the garnet field followed by 11% melting in the spinel field. This peridotite was then drawn up beneath the modern SW Indian Ridge, but produced little melt, largely in the garnet field due to the

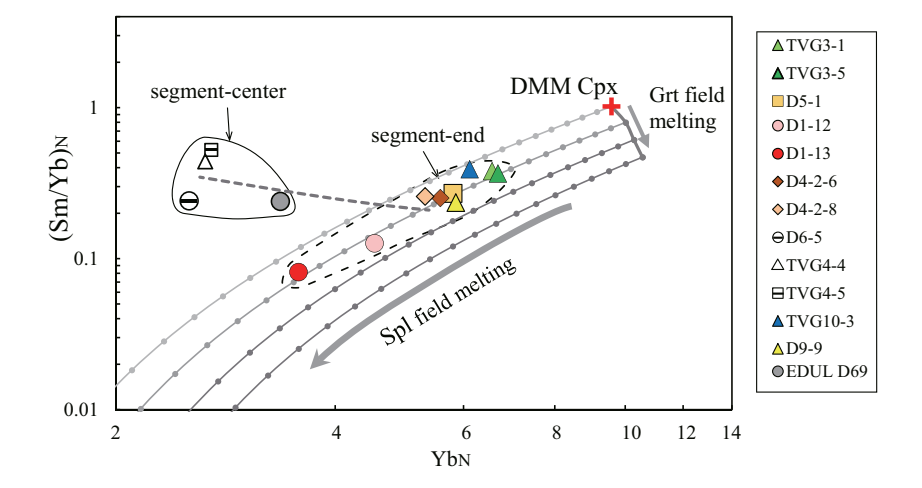


Fig. 11. Dragon Bone peridotite Cpx  $(Sm/Yb)_N$  versus  $Yb_N$ . Data represent the average of spot analyses for a sample. The thick grey line represents non-modal fractional melting of DMM (red cross, Salters and Stracke, 2004) in the garnet stability field. Subsequent melting in the spinel stability field is shown by three thin grey lines. Circles on curves represent 1% meltincrements. The dashed grey line presents the continuous open system melting path that starts at a residue – a product of 1% melting in the garnet field followed by 11% melting in the spinel field; this residue then underwent continuous open system melting induced by an enriched inflowing melt derived from 1% melting in the garnet field at influx melt rate  $\beta = 0.06$  ( $\beta$  is the proportion of melt added per unit of melting, Brunelli et al., 2014). Line ends when system reaches clinopyroxene exhaustion. Partition coefficients are from Salters and Longhi (1999) and Salters et al. (2002). Mineral modes and melt modes are the same as in Fig. 10.

prior depletion, resulting in amagmatic spreading at the modern ridge segment. As the mantle was pulled up higher in the mantle in the spinel stability field, it was subjected to the melt flux being produced beneath it by 1% melting in the garnet stability field. This produced the trend shown in Fig. 11 that crosses through the spinel field melting trends that matches the data for the segment center peridotites, as similarly found by Brunelli et al. (2014) for their sample D6–1-2.

# 5.3. Degree of partial melting of segment-end peridotites

The majority of Dragon Bone segment-end peridotites Cpx grains are nearly pure residues of melting as evidenced by both major and trace elements in Cpx (e.g., Cpx Na and Cr# contents in Fig. 9, REE patterns in Fig.8 and Ti—Zr covariations in Fig. 10). The degree of partial melting in the spinel stability field of a primitive upper mantle composition can be estimated through spinel Cr# (Hellebrand et al., 2001). Inferred from the average spinel Cr# of Dragon Bone peridotites, these peridotites have experienced 7–14% partial melting, calculated through  $F=10^{\rm *ln}$  (Cr#/100)  $\pm$  24, where F is degree of melting and Cr# is between 10 and 60 (Fig. 6; Hellebrand et al., 2001). Spinel compositions from D9–1, TVG3–1 and TVG3–3 plot at the low Cr# end of the global abyssal peridotite field (Dick and Bullen, 1984) and represent the lowest degree of depletion in this area.

 $(\bar{S}m/Yb)_N$  versus  $Yb_N$  variations are often used to identify whether before melting in the spinel stability field, the residual abyssal peridotites have experienced melting in the garnet stability field (e.g., Hellebrand et al., 2001; Johnson et al., 1990; Johnson and Dick, 1992). Here we use Sm/Yb ratios combined with Yb to model fractional melting of a DMM (Salters and Stracke, 2004), and to determine whether  $(Sm/Yb)_N$  -Yb $_N$  variations of the LREE-depleted Dragon Bone segment-end Cpx are consistent with their Ti–Zr variations.

The results show that all the LREE-depleted Dragon Bone segment-end samples, including those that show minor melt interaction, plot along a spinel field melting path after 1% of melting in the garnet stability field (Fig. 11). The samples along the spinel melting trend show no signs of melt-rock interactions, as melt-rock interaction would lead to a (Sm/Yb)<sub>N</sub> versus Yb<sub>N</sub> variations crosscutting the spinel melting trend (Brunelli et al., 2014; Seyler et al., 2018). In detail, the LREE-depleted Dragon Bone segment-end Cpx has relatively homogeneous (Sm/Yb)<sub>N</sub> ratios and Yb concentrations, again providing evidence of their residual character. Thus, the Sm/Yb)<sub>N</sub> versus Yb<sub>N</sub> variations of the Dragon Bone segment-end peridotites parallel to the spinel melting path suggest the last melting event occurred in the spinel field.

As shown in Fig. 11, the degree of melting in the garnet stability field is nearly constant at 1% for all the segment-end peridotites. This amount of depletion in the garnet stability field is consistent with the REE patterns, which are uniformly depleted in HREE and MREE (Fig. 8). These relatively uniform variations in the amount of depletion in the garnet stability field indicate that the differences in the degrees of depletion of these segment-end peridotites are mainly generated in the spinel stability field. Segment-center peridotites, however, have Sm/Yb ratios and concentrations that indicate a different melting process or source, as discussed in Section 5.2.3.

Based  $(Sm/Yb)_N-Yb_N$  variations all segment-end peridotites underwent a similar degree of melting in the garnet stability field (Fig. 11). The REE in combination with the spinel Cr# indicate that the near-axis peridotites (TVG3) underwent lower degree of melting (7–8%) in the spinel stability field than the segment-end off-axis peridotites (9–14%).

# 5.4. Ancient mantle depletion

The geologic observation of thin or no crust in this area (Zhou and Dick, 2013) is in contrast with the high degree of depletion of the peridotites. Under ultraslow spreading and cool lithosphere conditions,

melt extraction is expected to be low (e.g. Dick, 1989; Warren and Shimizu, 2010), which led Chen et al. (2015) to argue that melt was trapped in the mantle. Zhou and Dick (2013) and Gao et al. (2016) proposed that the modern ridge basalts are derived from a previously depleted mantle. This study shows that most Dragon Bone segment-end peridotites are residual in character and have little evidence for trapped melt in the mantle. The occurrence of peridotite at both the segment ends and the segment center indicates that recent melt production has been low. A previously depleted mantle, i.e., more depleted than a MORB mantle can be the cause for the sparse basaltic crust. It can explain the high degree of melting inferred from the peridotite Cpx REE patterns and spinel Cr# and the lack of observed crust. The major element variations of the Dragon Bone peridotites are also consistent with a two-stage depletion, thus offering additional evidence that the Dragon Bone mantle suffered ancient depletion. Considering the scarcity of crust at the ridge axis, only very limited amount of melting occurred during the second, low-pressure depletion event. Constraining the different proportions of degrees of melting in the ancient and recent event is difficult. While the total degree of melting in the spinel stability field was high, the earlier depletion event that evolved with garnet can also be deduced to have involved melting in the spinel stability field.

As illustrated in Fig. 11, the depletion in the garnet stability field was close to constant for all segment-end peridotites, and the amounts of melting in the spinel stability field were different. The ancient melting likely started at the same depth and temperature, and the amount of ancient depletion is similar for all the peridotites. This result indicates that these peridotites had similar source compositions during the recent depletion and that the relative differences in the degree of depletion of the peridotites are related to the recent depletion as opposed to the ancient depletion that involved garnet.

#### 5.5. Spatial-temporal evolution of partial melting of Dragon Bone mantle

Does this spatial variation in segment-end peridotites over tens of kilometers on the southern ridge flank express the variation in the mantle melting regime from past to present? To answer this question, we need to determine whether the off-axis peridotites are indeed older than the near-axis peridotites. Dick et al. (2010) argued that most abyssal peridotite samples from debris flows and talus ramps do not preserve key stratigraphic relations, so in general do not allow investigation of vertical composition gradients on a sub-kilometer scale (Dick et al., 2010 and references therein). The distance between off-axis and near-axis Dragon Bone peridotites is 20–50 km. Abyssal peridotites are commonly exposed on seafloor on rift valley walls, ridge ends, transform walls, detachment surfaces, and peridotite domes (e.g. Cann et al., 1997; Cannat and Seyler, 1995; Dick et al., 2010). The peridotites on the edge of the southern ridge flank, are distributed on rift mountains at distances 20-50 km away from the ridge axis (samples from dredges D5, D1 and D4-1) and the near-axis peridotites (from TVG3) are located at en-echelon domes about 10 km away from the axis. These samples do not occur near transform walls or detachment faults surfaces and the possibility that they are hanging wall debris can be excluded. Those samples located on the rift mountains are most likely in situ. En-echelon domes are generally associated with block faults exposing massive peridotites, as one of the seafloor extension modes on amagmatic ultraslow spreading ridges (Cannat et al., 2006). Peridotites collected by TV-grabs from tops of the peridotite domes, experienced little melting, consistent with this amagmatic spreading, and are also likely in-situ. A few hundred meters long high angle normal faults may also cut into the crust and expose ultramafic rocks (e.g., Dick et al., 2010; Francheteau et al., 1976), but such small normal faults won't disturb the sequence over distances of tens of kilometers. Therefore, the near-axis peridotites are younger than the offaxis peridotites tens of kilometers removed from the ridge. The exhumation age range of the near-axis samples is ~2 Myr, while that of the

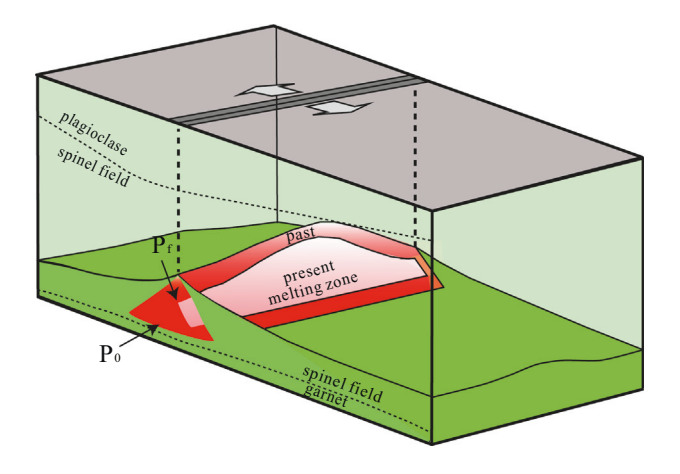


**Fig. 12.** 3D schematic diagram showing the decreased mantle melting zone during the recent depletion beneath the Dragon Bone segment. Past and present melting regimes under the SWIR are colored red and pink, respectively.  $P_0$  and  $P_f$  represent initial and final depths of partial melting. Also shown are the phase fields and the location of transform faults as two dashed lines on the front and back faces.

off-axis samples is ~4 to 8 Myr, assuming a constant half spreading rate of 6.5 km/Myr (Demets et al., 2010).

Samples from TVG3 have lower spinel Cr# and Cpx Cr# and higher Cpx Na and trace element abundances than the off-axis samples from D5, D1 and D4-2, among which the dredge D1 samples show the largest amount of depletion. These geochemical signatures indicate that samples from TVG3 have seen a lower degree of melting than those from D5, D1 and D4–2. This interpretation is also confirmed by their (Sm/ Yb)<sub>N</sub> versus Yb<sub>N</sub> variations. As argued already, the differences in the degree of partial melting between these segment-end peridotites were mostly caused during the recent melting process. Assuming a similar mantle composition beneath the Dragon Bone segment end through time, the near-axis peridotites have experienced a lower degree of partial-melting than the off-axis peridotites during the recent melting event, reflecting a shorter distance between the initial and final melting depths at present than in the past (Fig. 12). As the initial melting depth would be shallower in a cooler homogeneous mantle (Langmuir and Forsyth, 2007), the Dragon Bone mantle is argued to have been hotter in the past than at present. For the Dragon Bone segment-center peridotites, as they are quite uniform in characteristics that are less affected by metasomatism, e.g., spinel Cr# and HREE abundances, the melting history of segment-center peridotite can be deduced not to vary much through time. Thus, the melting regime beneath the Dragon Bone segment is presently smaller than it was in the past, and the decrease occurred in the spinel stability field (Fig. 12).

#### 6. Conclusions

We find on the basis of in-situ analysis of mineral major and trace elements that the Dragon Bone segment peridotites are the residues of two separate unrelated melting events. As a consequence, the amount of melt produced recently beneath the present day ridge axis was very low. Cpx trace elements show that Dragon Bone segment-center peridotites are only very locally affected by melt reaction. The melting regime beneath the Dragon Bone segment also progressively shrank over the last ten million years, creating an amagmatic spreading center. The earlier mantle-melting event represents an ancient depletion at higher pressures, while the subsequent ridge event involved melting and depletion at lower pressures in the spinel peridotite facies.

Supplementary data to this article can be found online at https://doi.org/10.1016/j.lithos.2018.11.014.

#### Acknowledgements

We express our gratitude to G. White, S. Yang, S. Henrick, B. Mayer and N. Waeselmann for their assistance in analyses at the National High Magnetic Field Laboratory and Y. Ai for major elements analyzes at the Analytical Laboratory of Beijing Research Institute of Uranium Geology. We very much appreciate the guidance of M. Humayun in data processing. We also thank the crew and scientists of RV *Dayang Yihao* Cruise 21, 30 and 34. These cruises were supported by China Ocean Mineral Resources Research and Development Association (COMRA) and organized by Second Institute of Oceanography, SOA. This work was supported by the Chinese National Key Basic Research Program (2012CB417300). HD was supported by the US National Science Foundation Grants 1434452, and 8608143; VS was supported by NSF grant 0930429. The NHMFL is supported by the National Science Foundation through NSF/DMR-1157490 and the State of Florida.

#### References

Anders, E., Grevesse, N., 1989. Abundances of the elements: Meteoritic and solar. Geochim. Cosmochim. Acta 53, 197–214.

Bédard, J.H., 2014. Parameterizations of calcic clinopyroxene—melt trace element partition coefficients. Geochem. Geophys. Geosyst. 15 (2), 303–336.

Bodinier, J.L., Vasseur, G., Vernieres, J., Dupuy, C., Fabries, J., 1990. Mechanisms of mantle metasomatism: geochemical evidence from the Lherz orogenic peridotite. J. Petrol. 31 (3), 597–628.

Brunelli, D., Seyler, M., Cipriani, A., Ottolini, L., Bonatti, E., 2006. Discontinuous melt extraction and weak refertilization of mantle peridotites at the Vema lithospheric section (Mid-Atlantic Ridge). J. Petrol. 47 (4), 745–771.

Brunelli, D., Paganelli, E., Seyler, M., 2014. Percolation of enriched melts during incremental open-system melting in the spinel field: a REE approach to abyssal peridotites from the Southwest Indian Ridge. Geochim. Cosmochim. Acta 127 (3), 190–203.

Cann, J.R., Blackman, D.K., Smith, D.K., McAllister, E., Janssen, B., Mello, S., Avgerinos, E., Pascoe, A.R., Escartin, J., 1997. Corrugated slip surfaces formed at ridge-transform intersections on the Mid-Atlantic Ridge. Nature 385, 329–332.

Cannat, M., Seyler, M., 1995. Transform tectonics, metamorphic plagioclase and amphibolitization in ultramafic rocks of the Vema transform fault (Atlantic Ocean). Earth Planet. Sci. Lett. 133 (3–4), 283–298.

Cannat, M., Rommevaux-Jestin, C., Sauter, D., Deplus, C., Mendel, V., 1999. Formation of the axial relief at the very slow spreading Southwest Indian Ridge (49° to 69°E). J. Geophys. Res. 104 (B10), 22,825–822,843.

Cannat, M., Sauter, D., Mendel, V., Ruellan, E., Okino, K., Escartin, J., Combier, V., Baala, M., 2006. Modes of seafloor generation at a melt-poor ultraslow-spreading ridge. Geology 34 (7), 605–608.

Chen, L., Chu, F.Y., Zhu, J.H., Dong, Y.H., Yu, X., Li, Z.G., Tang, L.M., 2015. Major and trace elements of abyssal peridotites: evidence for melt refertilization beneath the ultraslow-spreading Southwest Indian Ridge (53° E segment). Int. Geol. Rev. 57 (13), 1715–1734.

Cheng, H., Zhou, H., Yang, Q., Zhang, L., Ji, F., Dick, H.J.B., 2016. Jurassic zircons from the Southwest Indian Ridge. Sci. Rep. 6, 26260.

Collier, M.L., Kelemen, P.B., 2010. The case for reactive crystallization at mid-ocean ridges. J. Petrol. 51 (9), 1913–1940.

Demets, C., Gordon, R.G., Argus, D.F., 2010. Geologically current plate motions. Geophys. J. Int. 181 (1), 1–80. https://doi.org/10.1111/j.1365-246X.2009.04491.x.

Dick, H.J.B., 1977. Partial melting in the Josephine peridotite I, the effect on mineral composition and its consequence for geobarometry and geothermometry. Am. J. Sci. 277, 801–832.

Dick, H.J.B., 1989. Abyssal peridotites, very slow spreading ridges and ocean ridge magmatism. Geol. Soc. Lond. Spec. Publ. 45 (1), 71–105.

Dick, H.J.B., Bullen, T., 1984. Chromian spinel as a petrogenetic indicator in abyssal and alpinetype peridotites and spatially associated lavas. Contrib. Mineral. Petrol. 86 (1), 54–76.

Dick, H.J.B., Natland, J.H., 1996. Late-stage melt evolution and transport in the shallow mantle beneath the East Pacific rise. In: Mével, C., Gillis, K.M., Allan, J.F., Meyer, P.S. (Eds.), Proceedings of the Ocean Drilling Program, Scientific Results 147. College Station, TX, pp. 103–134.

Dick, H.J.B., Zhou, H., 2015. Ocean rises are products of variable mantle composition, temperature and focused melting. Nat. Geosci. 8 (1), 68–74. https://doi.org/10.1038/nge02318

Dick, H.J.B., Fisher, R.L., Bryan, W.B., 1984. Mineralogic variability of the upper most mantle along mid-ocean ridges. Earth Planet. Sci. Lett. 69, 88–106.

Dick, H.J.B., Lin, J., Schouten, H., 2003. An ultraslow-spreading class of ocean ridge. Nature 426 (6965), 405–412.

Dick, H.J.B., Lissenberg, C.J., Warren, J.M., 2010. Mantle melting, melt transport, and delivery beneath a slow-spreading ridge: the Paleo-MAR from 23°15′N to 23°45′N. J. Petrol. 51 (1–2), 425–467. https://doi.org/10.1093/petrology/egp088.

Dijkstra, A.H., Barth, M.G., Drury, M.R., Mason, P.R., Vissers, R.L., 2003. Diffuse porous melt flow and melt-rock reaction in the mantle lithosphere at a slow-spreading ridge: a structural petrology and LA-ICP-MS study of the Othris Peridotite Massif (Greece). Geochem. Geophys. Geosyst. 4 (8).

Field, S.W., Haggerty, S.E., 1994. Symplectites in upper mantle peridotites: development and implications for the growth of subsolidus garnet, pyroxene and spinel. Contrib. Mineral. Petrol. 118 (2), 138–156.

- Francheteau, J., Choukroune, P., Hékinian, R., Le Pichon, X., Needham, H.D., 1976. Oceanic fracture zones do not provide deep sections in the crust. Can. J. Earth Sci. 13, 1223–1235.
- Frisby, C., Bizimis, M., Mallick, S., 2016a. Hf-Nd isotope decoupling in bulk abyssal peridotites due to serpentinization. Chem. Geol. 440, 60–72.
- Frisby, C., Bizimis, M., Mallick, S., 2016b. Seawater-derived rare earth element addition to abvssal peridotites during serpentinization. Lithos 248–251, 432–454.
- Gao, C., Dick, H.J.B., Liu, Y., Zhou, H., 2016. Melt extraction and mantle source at a South-west Indian Ridge Dragon Bone amagmatic segment on the Marion rise. Lithos 246-247 (1), 48–60.
- Hellebrand, E., Snow, J.E., 2003. Deep melting and sodic metasomatism underneath the highly oblique-spreading Lena Trough (Arctic Ocean). Earth Planet. Sci. Lett. 216 (3), 283–299.
- Hellebrand, E., Snow, J.E., Dick, H.J., Hofmann, A.W., 2001. Coupled major and trace elements as indicators of the extent of melting in mid-ocean-ridge peridotites. Nature 410 (6829), 677–681.
- Hellebrand, E., Snow, J.E., Hoppe, P., Hofmann, A.W., 2002. Garnet-field melting and latestage refertilization in 'residual' abyssal peridotites from the Central Indian Ridge. J. Petrol. 43 (12), 2305–2338.
- Humayun, M., Davis, F.A., Hirschmann, M.M., 2010. Major element analysis of natural silicates by laser ablation ICP-MS. J. Anal. At. Spectrom. 25 (7), 998–1005.
- Jochum, K.P., Weis, U., Stoll, B., Kuzmin, D., Yang, Q., Raczek, I., Jacob, D., Stracke, A., Birbaum, K., Frick, D., Günther, D., Enzweiler, J., 2015. Determination of reference values for NIST SRM 610–617 glasses following ISO guidelines. Geostand. Geoanal. Res. 35 (4), 397–429.
- Johnson, K.T.M., 1998. Experimental determination of partition coefficients for rare earth and high-field-strength elements between clinopyroxene, garnet, and basaltic melt at high pressures. Contrib. Mineral. Petrol. 133 (1–2), 60–68.
- Johnson, K.T.M., Dick, H.J.B., 1992. Open system melting and temporal and spatial variation of peridotite and basalt at the Atlantis II Fracture Zone. J. Geophys. Res. Solid Earth 97 (B6), 9219–9241.
- Johnson, K.T.M., Dick, H.J.B., Shimizu, N., 1990. Melting in the oceanic upper mantle: an ion microprobe study of diopsides in abyssal peridotites. J. Geophys. Res. Solid Earth 95 (B3), 2661–2678.
- Langmuir, C.H., Forsyth, D.W., 2007. Mantle melting beneath mid-ocean ridges. Oceanography 20 (1), 78–89.
- Li, J., Jian, H., Chen, J., Singh, S.C., Aiguo, R., Qiu, X., Zhao, M., Wang, X., Niu, X., Ni, J., 2015. Seismic observation of an extremely magmatic accretion at the ultraslow spreading Southwest Indian Ridge. Geophys. Res. Lett. 42, 2656–2663.
- Liang, Y., Sun, C., Yao, L., 2013. A REE-in-two-pyroxene thermometer for mafic and ultra-mafic rocks. Geochim. Cosmochim. Acta 102 (2), 246–260.
- Longhi, J., 2002. Some phase equilibrium systematics of lherzolite melting: I. Geochem. Geophys. Geosyst. 3 (3), 1–33.
- Mallick, S., Dick, H.J.B., Sachi-Kocher, A., Salters, V.J.M., 2014. Isotope and trace element insights into heterogeneity of subridge mantle. Geochem. Geophys. Geosyst. 15 (6), 2438–2453.
- Mendel, V., Sauter, D., Parson, L., Vanney, J.R., 1997. Segmentation and morphotectonic variations along a super slow-spreading center: the Southwest Indian Ridge (57°E-70°E). Mar. Geophys. Res. 19 (6), 505–533.
- Menzies, M., 1973. Mineralogy and partial melt textures within an ultramafic-mafic body, Greece. Contrib. Mineral. Petrol. 42, 273–285.
- Navon, O., Stolper, E., 1987. Geochemical consequences of melt percolation: the upper mantle as a chromatographic column. J. Geol. 285–307.
- Niu, Y., 2004. Bulk-rock major and trace element compositions of abyssal peridotites: implications for mantle melting, melt extraction and post-melting processes beneath mid-ocean ridges. J. Petrol. 45 (12), 2423–2458.
- Niu, X., Ruan, A., Li, J., Minshull, T.A., Sauter, D., Wu, Z., Qiu, X., Zhao, M., Chen, J., Singh, S., 2015. Along-axis variation in crustal thickness at the ultraslow spreading Southwest Indian Ridge (50°E) from a wide-angle seismic experiment. Geochem. Geophys. Geosyst. 16, 468–485.
- Reed, S.J.B., 2005. Electron Microprobe Analysis and Scanning Electron Microscopy in Geology. Cambridge University Press.
- Salters, V.J.M., Dick, H.J.B., 2002. Mineralogy of the mid-ocean-ridge basalt source from neodymium isotopic composition of abyssal peridotites. Nature 418 (6893), 68–72.
- Salters, V.J.M., Longhi, J.E., 1999. Trace element partitioning during the initial stages of melting beneath mid-ocean ridges. Earth Planet. Sci. Lett. 166, 15–30.
- Salters, V.J.M., Longhi, J.E., 2004. Composition of the depleted mantle. Geochem. Geophys. Geosyst. 5.

- Salters, V.J.M., Longhi, J.E., Bizimis, M., 2002. Near mantle solidus trace element partitioning at pressures up to 3.4 GPa. Geochem. Geophys. Geosyst. 3 (7), 1–23.
- Sauter, D., Patriat, P., Rommevaux-Jestin, C., Cannat, M., Briais, A., 2001. The Southwest Indian Ridge between 49°15′E and 57°E: focused accretion and magma redistribution. Earth Planet. Sci. Lett. 192, 303–317.
- Seyler, M., Brunelli, D., 2018. Sodium chromium covariation in residual clinopyroxenes from abyssal peridotites sampled in the 43°-46°E region of the Southern Indian Ridge. Lithos 302-303. 142-157.
- Seyler, M., Toplis, M.J., Lorand, J.P., Luguet, A., Cannat, M., 2001. Clinopyroxene microtextures reveal incompletely extracted melts in abyssal peridotites. Geology 29 (2), 155–158.
- Seyler, M., Cannat, M., Mével, C., 2003. Evidence for major element heterogeneity in the mantle source of abyssal peridotites from the Southwest Indian Ridge (52° to 68°E). Geochem. Geophys. Geosyst. 4 (2).
- Seyler, M., Lorand, J.-P., Toplis, M.J., Godard, G., 2004. Asthenospheric metasomatism beneath the mid-ocean ridge: evidence from depleted abyssal peridotites. Geology 32 (4) 301–304
- Seyler, M., Lorand, J.-P., Dick, H.J.B., Drouin, M., 2007. Pervasive melt percolation reactions in ultra-depleted refractory harzburgites at the Mid-Atlantic Ridge, 15° 20′ N: ODP Hole 1274A. Contrib. Mineral. Petrol. 153 (3), 303–319.
- Seyler, M., Brunelli, D., Toplis, M.J., Mével, C., 2011. Multiscale chemical heterogeneities beneath the eastern Southwest Indian Ridge (52°E-68°E): Trace element compositions of along-axis dredged peridotites. Geochem. Geophys. Geosyst. 12, Q0AC15.
- Shimizu, Y., Arai, S., Morishita, T., Ishida, Y., 2008. Origin and significance of spinel-pyroxene symplectite in lherzolite xenoliths from Tallante, SE Spain. Mineral. Petrol. 94 (1–2), 27–43.
- Snow, J.E., Dick, H.J.B., 1995. Pervasive magnesium loss by marine weathering of peridotite. Geochim. Cosmochim. Acta 59, 4219–4235.
- Standish, J.J., Dick, H.J.B., Michael, P.J., Melson, W.G., O'Hearn, T., 2008. MORB generation beneath the ultraslow-spreading Southwest Indian Ridge (9°-25°E): Major element chemistry and the importance of process versus source. Geochem. Geophys. Geosyst. 9.
- Stracke, A., Snow, J.E., Hellebrand, E., Handt, A.V.D., Bourdon, B., Birbaum, K., Günther, D., 2011. Abyssal peridotite Hf isotopes identify extreme mantle depletion. Earth Planet. Sci. Lett. 308 (3), 359–368.
- Suhr, G., Seck, H.A., Shimizu, N., Günther, D., Jenner, G., 1998. Infiltration of refractory melts into the lowermost oceanic crust: evidence from dunite- and gabbro-hosted clinopyroxenes in the Bay of Islands Ophiolite. Contrib. Mineral. Petrol. 131 (2–3), 136–154.
- Suhr, G., Kelemen, P., Paulick, H., 2008. Microstructures in Hole 1274a peridotites, ODP Leg 209, Mid-Atlantic Ridge: tracking the fate of melts percolating in peridotite as the lithosphere is intercepted. Geochem. Geophys. Geosyst. 9 (3) Q03012.
- Sun, C., Liang, Y., 2012. Distribution of REE between clinopyroxene and basaltic melt along a mantle adiabat: effects of major element composition, water, and temperature. Contrib. Mineral. Petrol. 163 (5), 807–823.
- Tao, C., Lin, J., Guo, S., Chen, J., Wu, G., Han, X., German, C.R., Yoerger, D.R., Zhou, N., Li, H., et al., 2012. First active hydrothermal vents on an ultraslow-spreading center: Southwest Indian Ridge. Geology 40 (1), 47–50.
- Walter, M.J., 1998. Melting of garnet peridotite and the origin of komatiite and depleted lithosphere. J. Petrol. 39 (1), 29–60.
- Warren, J.M., 2016. Global variations in abyssal peridotite compositions. Lithos 248-251, 193-219.
  Warren, J.M., Shimizu, N., 2010. Cryptic variations in abyssal peridotite compositions: evidence for shallow-level melt infiltration in the oceanic lithosphere. J. Petrol. 51 (1-2) 305-473
- Wasylenki, L.E., Baker, M.B., Kent, A.J.R., Stolper, E.M., 2003. Near-solidus melting of the shallow upper mantle: partial melting experiments on depleted peridotite. J. Petrol. 44 (7), 1163–1191.
- Yang, S., Humayun, M., Righter, K., Jefferson, G., Fields, D., Irving, A.J., 2015. Siderophile and chalcophile element abundances in shergottites: Implications for Martian core formation. Meteorit. Planet. Sci. 50 (4), 691–714.
- Zhao, M., Qiu, X., Li, J., Ruan, A., Chen, J., Cannat, M., Singh, S., Zhang, J., Wu, Z., Niu, X., 2013. Three-dimensional seismic structure of the Dragon Flag oceanic core complex at the ultraslow spreading Southwest Indian Ridge (49°39′E). Geochem. Geophys. Geosyst. 14 (10). 4544–4563.
- Zhou, H., Dick, H.J.B., 2013. Thin crust as evidence for depleted mantle supporting the Marion rise. Nature 494 (7436), 195–200.